AIAA JOURNAL
Vol. 48, No. 12, December 2010

High-Lift Airfoil Separation with Dielectric Barrier Discharge Plasma Actuation

Jesse Little*
University of Arizona, Tucson, Arizona 85721
and
Mo Samimy†
Ohio State University, Columbus, Ohio 43235

DOI: 10.2514/1.J050452

The efficacy of a single dielectric barrier discharge plasma actuator for controlling turbulent boundary-layer separation from the deflected flap of a high-lift airfoil is investigated between Reynolds numbers of 240,000 (15 m/s) and 750,000 (45 m/s). Momentum coefficients for the dielectric barrier discharge plasma actuator are approximately an order of magnitude lower than those usually employed for such studies, yet control authority is still realized through amplification of natural vortex shedding from the flap shoulder, which promotes momentum transfer between the freestream and separated region. This increases dynamic loading on the flap and further organizes turbulent fluctuations in the wake. The measured lift enhancement is primarily due to upstream effects from increased circulation around the entire model, rather than full reattachment to the deflected flap surface. Lift enhancement via instability amplification is found to be relatively insensitive to changes in angle of attack, provided that the separation location and underlying dynamics do not change. The modulation waveform used to excite low-frequency perturbations with a high-frequency plasma-carrier signal has a considerable effect on the actuator performance. Control authority decreases with increasing Reynolds number and flap deflection, highlighting the necessity for further improvement of plasma actuators for use in realistic takeoff and landing transport aircraft applications. These findings are compared to studies on a similar high-lift platform using piezoelectric-driven zero-net-mass flux actuation.

Nomenclature

C_D	=	sectional drag coefficient
C_{dp}	=	sectional pressure drag coefficient
C_E	=	power coefficient, $P/q_\infty U_\infty c$
C_L	=	sectional lift coefficient
C_P	=	pressure coefficient
C_μ	=	momentum coefficient, $J/q_\infty c$
$\langle C_\mu \rangle$	=	oscillatory momentum coefficient, $\langle J \rangle / q_\infty c$
$C_{\mu,\mathrm{tot}}$	=	total momentum coefficient, $C_\mu + \langle C_\mu \rangle$
c	=	model chord, 25.4 cm
c_p	=	fluctuating pressure coefficient
F^*	=	normalized modulation frequency, f_m/f_{TE}
F_c^+	=	reduced frequency based on model chord, fc/U_∞
F_L^+	=	reduced frequency based on flap length, fL/U_∞
$F_{L,m}^+$	=	reduced modulation frequency based on flap length, $f_m L/U_\infty$
f	=	frequency
f_m	=	modulation frequency
f_{TE}	=	characteristic frequency measured on the flap
H	=	shape factor, δ^*/θ
J	=	time-averaged actuator-induced momentum, $\int_0^\infty \rho U^2 \, \mathrm{d}y$
$\langle J \rangle$	=	oscillatory actuator-induced momentum, $\int_0^\infty \rho U_{\mathrm{rms}}^2 \, \mathrm{d}y$
L	=	flap length, 6.35 cm
P	=	time-averaged power consumed by plasma
q_∞	=	freestream dynamic pressure, $\rho U_\infty^2/2$
Re	=	chord-based Reynolds number, $U_\infty c/\nu$
R_{vv}	=	spatial correlation coefficient of v
U	=	streamwise velocity
$\bar{U}$	=	time-averaged streamwise velocity
U_{rms}	=	root mean square of streamwise velocity
U_∞	=	freestream velocity
V	=	vertical velocity
$\bar{V}$	=	time-averaged vertical velocity
v	=	fluctuating vertical velocity
x/c	=	normalized streamwise coordinate
y/c	=	normalized vertical coordinate
y_T	=	y/c coordinate of the tail of the deflected trailing-edge flap
α	=	angle of attack, deg
Δx	=	spatial resolution,
δ_f	=	flap deflection angle, deg
δ^*	=	boundary-layer displacement thickness
θ	=	boundary-layer momentum thickness
ν	=	kinematic viscosity
ρ	=	density
Ω	=	phase-averaged spanwise vorticity
$\bar{\Omega}$	=	time-averaged spanwise vorticity
Ω^*	=	normalized spanwise vorticity, $\Omega c/U_\infty$

Presented as Paper 2010-1088 at the AIAA 48th Aerospace Sciences Meeting, Orlando, FL, 4–7 January 2010; received 22 January 2010; revision received 12 August 2010; accepted for publication 15 August 2010.

*Assistant Professor, Department of Aerospace and Mechanical Engineering. Member AIAA.
†Howard D. Winbigler Professor of Engineering, Department of Mechanical Engineering; samimy.1@osu.edu. Fellow AIAA (Corresponding Author).

I. Introduction

HIGH-LIFT airfoils typically employ trailing-edge (TE) flaps that can be deflected during takeoff or landing and stowed during cruise. Such devices enhance the lift of conventional airfoils, but can impose a penalty, due to flow separation that occurs when the momentum of fluid in the boundary layer is not sufficient to overcome wall friction and the adverse pressure gradient encountered as it travels over the deflected flap surface. Traditional methods of eliminating flow separation on high-lift airfoils use passive flow control (PFC) technology in the form of multi-element flaps that allow mixing of fluid between the pressure and suction sides. These

systems are effective for augmenting lift, but create substantial increases in mechanical complexity, manufacturing cost, weight and parasitic drag, even when stowed during cruise. A system study indicates that significant decreases in manufacturing cost, weight and drag could be realized if the complex multi-element high-lift system is simplified while maintaining $C_{L,\max}$ [1]. To obtain similar performance, PFC in the form of the slots must then be replaced by some active flow control (AFC) device that would not reintroduce similar or additional detrimental factors such as manufacturing cost and increased power consumption. The benefits of such a simplification have fueled two major research projects in this area. The ADVINT program on the Boeing tilt-wing supershort takeoff and landing transport [2–7] and a parallel work by NASA [8–13] have produced significant developments using AFC via both nonzero and zero-net-mass flux (ZNMF) periodic excitation [14], which is well established in the flow control community [15]. Some of the pertinent findings of these programs with respect to lift enhancement are relevant to this paper and warrant mention here.

1) The control authority for a given flap deflection δ_f is highly sensitive to actuation location in regions of high surface curvature encountered near the flap shoulder [11]. This is especially true for typical ZNMF-type actuation issuing from small, often 2-D, slots on the model surface. Such results can be traced back to the importance of separation location on the actuator placement, in that control introduced at or slightly upstream of the separation point generally produces the greatest effect [15].

2) High-frequency excitation ($F^+ > 10$) is less efficient in terms of both momentum and power than low-frequency modulated versions of the same signal at $F^+ \sim 0.3$–1.5 [11,16]. The latter mechanism relies on the existence of natural instabilities in the flowfield that can selectively amplify small disturbances if introduced near a region of strong receptivity [17].

3) In either the low- or high-frequency-forcing cases above, amplifying the disturbance generally serves to increase the control authority [3,11,12], but the scaling laws governing these effects are not well defined [14].

4) When controlling flow over deflected flaps on airfoils, separation control and circulation control are inherently linked. Increases in C_L are often realized from upstream effects due to enhanced circulation, rather than complete or partial reattachment to the flap surface [3,11,18]. This is especially true for low-frequency forcing ($F^+ \sim 0.3$–1.5), during which separation is not radically delayed [9]. Such behavior does not occur in studies of separation control for wall-mounted humps [19].

This work uses a platform similar to NASA's to study the efficacy of DBD plasma actuators for controlling TE separation. The recent interest in plasma actuators for aerodynamic flow control is motivated by their simple construction, lack of moving parts, high bandwidth, and ease of implementation. Because of these amenable characteristics, researchers have investigated their application in a variety of flow control problems, particularly those associated with airfoil leading-edge (LE) flow separation. These studies and the current state of the DBD plasma knowledge base are summarized in various review articles [20,21]. While the potential of plasma-based actuation for separation control is apparent, it also possesses some drawbacks. DBD plasma actuators have primarily been limited to use in relatively low-speed ($U_\infty < 30$ m/s) low Reynolds number ($\sim 10^5$) applications, such as those associated with micro air vehicles, due to the weak flows induced by the plasma discharge [20,22]. To date, DBD plasma actuators have not produced sufficient momentum to eliminate separation for flows over simple flaps at $Re > 10^5$ unless the freestream velocity and is quite low [23], although novel arrangements of these devices show promise [24]. Recent archival publications suggesting momentum production can be increased by an order of magnitude using thicker dielectric materials with lower dielectric constants, and higher ac voltages imply that the technology is continuing to mature [25]. Research is also underway for alternative methods of generating DBD plasma actuation that rely on high-voltage nanosecond pulses [26–28]. Such devices appear to accomplish control based on thermal effects alone, similar to arc-filament-based plasma actuators [29].

The following sections present results of an experimental study of DBD plasma for controlling TE separation on a scaled simplified version of the NASA airfoil model. The publications on high-lift airfoil studies listed above provide a benchmark for comparing the performance and efficacy of DBD plasma for this very challenging AFC problem. Results demonstrate both the positive and negative aspects of using of a single ac-driven DBD plasma actuator for controlling separation over a deflected TE flap.

II. Actuator Background

The ac-driven DBD plasma actuator for aerodynamic flow control is composed of two electrodes separated by a dielectric material arranged in an asymmetric fashion (Fig. 1) [20,21]. Application of a sufficiently high-voltage ac signal between the electrodes weakly ionizes the air over the dielectric covering the encapsulated electrode. The dielectric barrier allows the generation of a large volume of plasma by preventing the discharge from collapsing into an arc. The DBD plasma actuator is a self-limiting device, in that the accumulation of charged particles onto the dielectric surface opposes the electric field, requiring progressively higher voltages to sustain the discharge. This is circumvented using an ac waveform, which, because of a change in polarity, creates movement of charged species back and forth between the exposed electrode and the dielectric surface at the ac driving frequency. The movement of these charged particles transfers momentum to the flow via electron/ion-neutral collisions. In quiescent conditions, the asymmetric plasma actuator creates suction above the exposed electrode and a more dominant pseudo wall jet over, and downstream of, the covered electrode whose strength varies with dielectric properties, voltage, frequency, and waveform [30]. The induced flow/ionic wind is predominantly directed away from the exposed electrode toward the covered electrode. This occurs due to the asymmetry of the actuator geometry and behavior of the discharge over the two waveform half-cycles. The movement of negative species away from the exposed electrode dominates the momentum transfer in air [31] and is particularly dependent on oxygen content [32,33].

As with other methods of periodic excitation [15], ac-driven DBD plasma actuators are often most effective for separation control and lift enhancement when excitation is created with reduced frequency F^+ on the order of unity, where the length scale used to define F^+ is the length of the separation zone [22,34,35]. To operate in this fashion, the actuator is generally excited with a 1–10 kHz carrier frequency that is optimized for flow generation based on the bulk capacitance of the actuator [21]. The high-frequency signal is then modulated at a lower frequency to excite the longer wavelength instabilities associated with separated-flow dynamics (Fig. 2). This behavior is analogous to ZNMF-type actuation created by piezoelectric diaphragms, which produce the highest-intensity

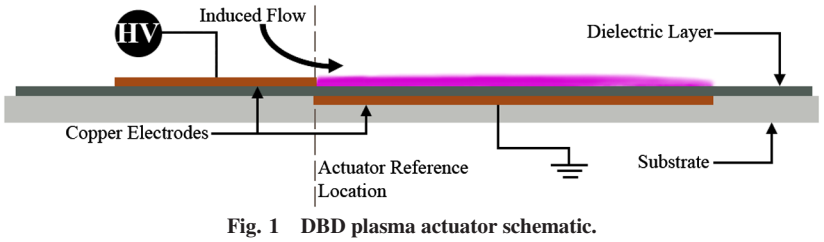

Fig. 1 DBD plasma actuator schematic.

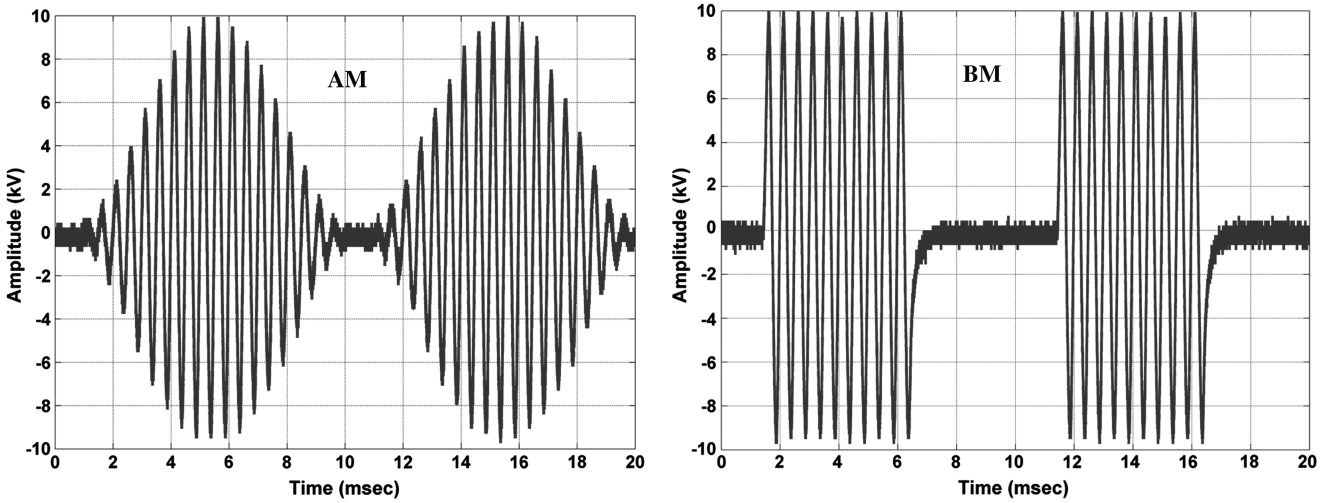

Fig. 2 Example waveforms for amplitude modulation with modulation index of 1 (AM) and burst modulation (BM) at 50% duty cycle of the DBD plasma-carrier frequency.

fluctuations when excited near the resonant frequency of the disc and/or cavity, which is often on the order of a few kilohertz. Often, studies of separation control with DBD plasma actuators assume that the flow does not feel perturbations created by the high-frequency carrier signal, but instead responds as if exposed to a steady wall jet [36]. For many low-speed applications, this is true because the instabilities involved are not receptive to high-frequency perturbations and instead feel their effect as a quasi-steady phenomenon. However, it has been confirmed that in air, the movement of charged species in the plasma creates a dominant perturbation at the carrier frequency of plasma generation and thus suggests the possibility of using DBD plasma actuators for high-frequency-forcing applications [37] if sufficient amplitude can be produced [31,33,38,39].

In terms of frequency and the excitation signals, piezoelectric and DBD plasma actuators are quite similar, but the characteristics of the momentum production and delivery are fundamentally different. In a typical ZNMF-type actuator, periodic blowing and suction is 180° out of phase and occurs through a slot or orifice mounted at an angle relative to the freestream or aerodynamic surface. DBD plasma actuators are completely surface-mounted, and the exact location at which the plasma actuator accomplishes control is not immediately obvious, although actuators placed at or slightly upstream of the separation location give favorable results [34,40,41]. This is consistent with modeling results that show that the highest-force density associated with such devices is near the edge of the exposed electrode adjacent to the plasma formation [42,43]. As described above, there are periodic blowing and suction effects for a DBD plasma actuator, but these predominantly occur at the same phase of the input waveform, do not emanate from a common location (i.e., slot), and are far from equal in magnitude. This behavior causes DBD plasma actuators to perform more similarly to a wall-jet-producing pulsed-blowing device, while still retaining ZNMF properties.

Throughout this paper, we attempt to compare the performance of DBD plasma actuators to the piezoelectric-driven ZNMF actuator results of NASA for a scaled version of the same airfoil. Despite the impossibility of exactly replicating the test conditions and baseline behavior between the two projects, results show some very consistent trends that highlight the similarities between these two very different actuators for controlling TE flow separation.

III. Experiment

A. Wind Tunnel

A Gottingen-type, closed, recirculating wind tunnel with an optically accessible $61 \times 61 \times 122$ cm^3 ($2 \times 2 \times 4$ ft^3) test section serves as the test bed. Test-section walls are constructed of 25.4-mm-thick (1-in.-thick) super-abrasion-resistant acrylic. Each side wall is fitted with a 30.5-cm-diam (12-in.-diam) port that is located 30.5 cm (12 in.) from the test-section floor and 61 cm (24 in.) downstream of the test-section entrance. Airflow in the tunnel is continuously variable from 3–90 m/s (10–300 ft/s). Flow conditioning upstream of the test section includes a hexagonal cell aluminum honeycomb, and high-porosity stainless steel screens are mounted downstream of the test section as a safety catch. Four high-efficiency turning cascades fabricated of galvanized steel are installed in each of the four tunnel elbows. This assembly results in freestream turbulence levels of ~0.25% near the test-section inlet. The tunnel is also equipped with a commercial aluminum fin/copper tube, double-row heat exchanger with set-point controller, and electronic modulating valve. This arrangement allows the tunnel freestream operating temperature to be maintained within 1°C from the ambient when supplied with a sufficient source of cooling water [maximum 189 lpm (50 gpm)].

B. Airfoil Model

A simplified high-lift version of the NASA Energy Efficient Transport (EET) airfoil has been chosen as the test model. The 2-D EET airfoil has been thoroughly examined [44], but significant studies on AFC with ZNMF actuators have been completed for a similar simplified version [8–13]. The Ohio State University (OSU) version has a chord of 25.4 cm (10 in.) at $\delta_f = 0°$ and fully spans the 61 cm (24 in.) test section in a horizontal configuration. The model is equipped with a deflectable (0–60°) TE flap that is 25% of the airfoil chord but, for simplicity, lacks the LE droop used by NASA. It is constructed of a nylon compound (Duraform GF) and has been fabricated using selective laser sintering technology. Independent settings for α and δ_f are done manually using separate wall plugs. A photograph showing the airfoil with TE flap deflected and flap wall plug is shown in Fig. 3. Instrumentation in the model includes 45 static pressure taps located near the test-section centerline and 15 static pressure taps at $\frac{1}{4}$ and $\frac{3}{4}$ span. The model is also instrumented with seven high-bandwidth pressure transducers (Kulite XCQ-080

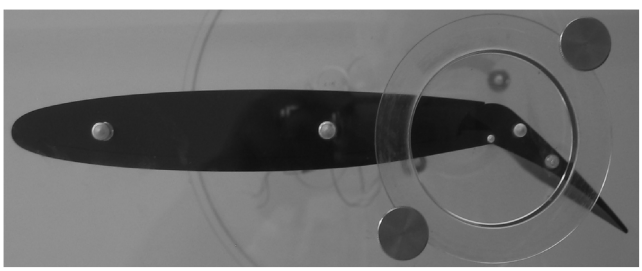

Fig. 3 OSU version of the simplified high-lift EET airfoil with trailing-edge flap deflected.

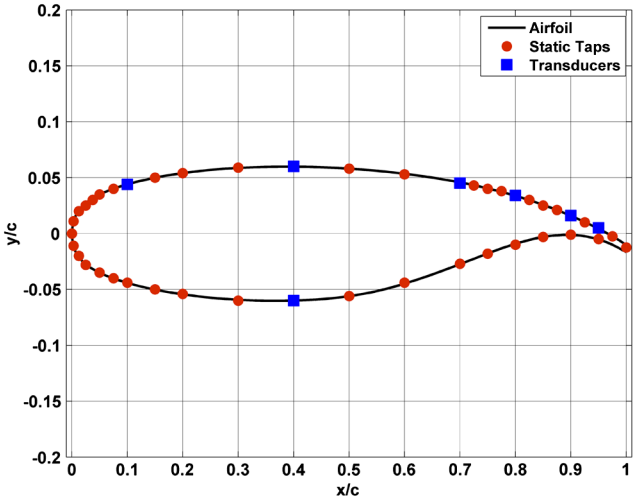

Fig. 4 2-D profile of the airfoil in cruise configuration ($\delta_f = 0$) showing the approximate location of static pressure taps and high-bandwidth pressure transducers near the airfoil centerline.

and LQ-062) flush-mounted on the model surface near the centerline. Figure 4 shows the airfoil profile and the location of static pressure taps and transducers.

C. DBD Plasma Actuator

Input signals for the DBD plasma actuators are generated using a dSpace DSP 1103 board and corresponding software. Signals generated by dSpace are used as inputs to a Powertron model 1500S ac power supply and step-up high-voltage transformer. Amplified signals are sent to a low-power (200 W) high-voltage (0–20 kV_{rms}) transformer designed to operate in the frequency range of 1–5 kHz. Voltage measurements are acquired and monitored at the secondary side of the high-voltage transformer with a Tektronix P6015A probe. The power dissipated by the actuator is calculated with the Lissajous figure using charge-voltage measurements [45]. A 47 nF capacitor is connected in series with the covered ground electrode in each case. The voltage across the capacitor is measured using a Tektronix P6111B voltage probe. The corresponding signals are monitored on a LeCroy Waverunner 6050A oscilloscope, but the actual power calculation is performed offline. In all cases presented, the DBD plasma actuators are operated at $\sim$20 kV_{pp}.

Actuators are composed of two copper tape electrodes separated by a Kapton tape dielectric (Fig. 1). There is a slight overlap between the electrodes to encourage uniform plasma generation. The covered ground electrode is 12.7 mm ($\frac{1}{2}$ in.) wide and the exposed high-voltage electrode is 6.35 mm ($\frac{1}{4}$ in.) wide. Both electrodes have a thickness of 0.09 mm (0.0035 in.). The dielectric barrier is composed of three layers of Kapton tape. Each layer has a thickness of 0.09 mm (0.0035 in.) and dielectric strength of 10 kV. The total thicknesses of the dielectric and the device as a whole are 0.27 mm (0.011 in.) and 0.44 mm (0.018 in.), respectively. The spanwise length of the discharge on the airfoil is constant and approximately 46 cm ($\sim$18 in.). Actuator locations are specified relative to the downstream edge of the exposed electrode and the device is adhered directly to the substrate.

D. Diagnostics

Measurements of static pressure from taps on the model surface are acquired using Scanivalve digital pressure sensor arrays (DSA-3217). Subsequent values of sectional C_P and integrated C_L are averaged over 50 samples acquired at 1 Hz. Pressure transducers are powered using an in-house-constructed signal conditioner. Low-pass hardware filtering is performed with an additional six-pole elliptic-type Kemo unit at cutoff frequency of 25 kHz. The resulting pressure traces are sampled simultaneously at 50 kHz using a National Instruments PCI-6143 data acquisition board. Average pressure spectra are calculated from 50 blocks of 8192 pressure samples, which results in a frequency resolution of approximately 6 Hz.

Two-component particle image velocimetry (PIV) is used to obtain quantitative measurements of the velocity fields in the airfoil wake, upstream boundary layer, and the actuator on a flat plate in still air. Images are acquired and processed using a LaVision PIV system. Nominally submicron olive oil seed particles are introduced upstream of the test-section contraction using a six-jet atomizer. A dual-head Spectra Physics PIV-400 Nd:YAG laser is used in conjunction with spherical and cylindrical lenses to form a thin light sheet that allows PIV measurements. The time separation between laser pulses used for particle scattering is tuned according to the flow velocity, camera magnification, and correlation window size. Two images corresponding to the pulses from each laser head are acquired by a LaVision 14-bit 2048 by 2048 pixel Imager Pro-X charge-couple-device camera equipped with a Nikon Nikkor 50 mm $f1.2$ lens. Boundary-layer and flat-plate PIV data are acquired using an additional 2× teleconvertor to increase spatial resolution. The wall plug arrangement requires that the camera view the laser from a downstream angle of approximately 14° in the airfoil-wake case. Data for the boundary layer and actuator in still air are acquired with the camera perpendicular to the light sheet. For each image pair, subregions are cross-correlated using decreasing window size (64^2–32^2 $pixel^2$) multipass processing with 50% overlap. An image-correction algorithm is applied to the data set, due to the non-orthogonal viewing angle in the airfoil-wake case. The resulting velocity fields are postprocessed to remove any spurious vectors using an allowable vector range and median filter. Removed vectors are replaced by an interpolation procedure using an average of all nonzero neighboring vectors. A 3×3 Gaussian smoothing filter is also applied to the calculated velocity fields. The PIV data are sampled at 10 Hz. Statistics for the airfoil wake, boundary layer, and actuator characterization are calculated from 1000, 500, and 500 instantaneous velocity fields, respectively.

Phase-locked PIV data in the airfoil wake are acquired using the programmable timing unit of the LaVision system. The acquisition is synced with the modulation frequency of the actuation signal. The baseline pressure signal is not sufficiently periodic to allow this acquisition in the airfoil case. Velocity fields at various phases of the actuator modulation frequency are investigated by stepping through the actuator period using time delays. The resulting phase-locked data sets are averaged over 100 images at each phase, which is found to be sufficient for resolving the primary features (velocity and vorticity) of the flowfields. Phase-locked PIV data are acquired at 5 Hz. The spatial resolutions of PIV data for the flat-plate, boundary-layer, and airfoil-wake data sets are approximately 0.2, 0.4, and 2.4 mm, respectively. Near-surface measurements for the flat-plate and boundary-layer data sets are obtained within 0.3 and 0.4 mm of the substrate, respectively.

Full-scale accuracy for measurements of instantaneous velocity and the uncertainty on mean velocity calculations are listed in Table 1. The former is calculated by assuming negligible laser timing errors and a correlation peak estimation error of 0.1 pixels. The smaller error in the boundary-layer and airfoil-wake cases is due to better choices of the time separation between laser pulses, due to the a priori knowledge of maximum velocities in the freestream flow. The uncertainties in measurements of mean velocity are presented using 95%-confidence intervals [46]. The values in Table 1 are in terms of relative error. The actuator and boundary-layer cases are estimated using the average standard deviation and average velocity in the near-wall profiles, which gives a more representative estimate than the maximum or freestream velocity. The uncertainty in the

Table 1 Uncertainty of PIV measurements

	$\bar{U}$	$\bar{V}$	U, V
Actuator characterization	4–6%	——	1.7%
Boundary layer	0.5–0.7%	——	0.9%
Airfoil wake	2–3%	2–3%	0.9%

airfoil wake is estimated using the maximum standard deviation in the turbulent wake and the freestream velocity. A range of values that encompasses all the flowfields surveyed is listed in the interest of brevity. The actuator and wake measurements have higher values of uncertainty, due to the unsteady natures of these flowfields. The V component of velocity has not been considered for the actuator and boundary-layer measurements, since it is not relevant to calculations of integral parameters.

E. Test Conditions

Experiments on controlling flow separation on the TE flap have been conducted for Reynolds numbers between 240,000 (15 m/s) and 750,000 (45 m/s) for δ_f of 20–40° at atmospheric temperature and pressure. These test conditions correspond to sample published results of NASA work [9,11], but do not contain studies on the effect of LE droop, which limits our analysis to lower α. For all airfoil measurements, data are acquired by establishing a separated-flow baseline condition then energizing the actuator. For repeated samples of different forcing cases, the baseline separated condition is reestablished between consecutive control cases to eliminate confusion on the results due to hysteresis effects. There is a nonnegligible blockage effect for some of the configurations outlined above. However, the majority of testing is performed at $\alpha = 0°$, for which all cases have less than 10% solid blockage. The C_L increase due to control is shown to be relatively independent of α below 6 deg. This, along with confirmation of a turbulent boundary layer approaching the flap, suggests that blockage should not have a great effect on the AFC performance. Thus, wind-tunnel corrections have not been performed under the pretext that they should be conserved across the test matrix.

IV. Results

A. Actuator Characterization

The velocity induced by a single DBD plasma actuator in still air has been characterized using PIV. The effect of seed particles on plasma-induced flow has been briefly examined and suggests that velocimetry techniques (PIV and laser Doppler velocimetry) may slightly underpredict the maximum plasma-induced flow in quiescent air [39]. However, our work shows similar control authority (ΔC_L), independent of whether seed particles are in the test section. The characterization is performed by mounting actuators on a flat-plate substrate made from the same material as the airfoil model. The length of the plasma actuator for characterization purposes is ~16 cm. To minimize surface reflections, the flat plate is mounted with its surface normal in the plane of the laser sheet orthogonal to the beam propagation direction. The plasma-induced flow has been measured for a range of forcing cases that encompass relevant excitation frequencies for TE control. Profiles of U and U_{rms} created by the actuator 20 mm downstream of the electrode interface are shown in Fig. 5. The profiles have been forced to obey a no-slip condition at the wall. Plasma generation at a frequency of 3000 Hz creates a wall jet with maximum mean velocity of ~3.5 m/s approximately 1 mm from the surface (Fig. 5a). Operating the actuator using burst modulation (BM) at 50% duty cycle (DC) lowers the maximum induced velocity but creates profiles that become substantially fuller as the burst frequency is decreased. This average velocity profile is consistent with a startup vortex and sustained unsteady vortex train widely observed in the literature for unsteady actuation [21,22,47,48]. The fluctuating behavior of BM actuation follows a similar trend in profile fullness, but the maximum value of the fluctuations now decreases with increasing frequency. This behavior is strongly dependent on the carrier frequency and DC, which have been previously discussed [47]. The profiles in Fig. 5 have been used to calculate both mean J/ρ and oscillatory $\langle J/\rho \rangle$ components of momentum [22] using a constant-density assumption [49]. The $x = 20$ mm location is chosen since it is near the discharge, but just outside the region where visible radiation from the discharge can contaminate the PIV data. It should be noted that the downstream location at which the momentum should be calculated for DBD plasma actuation is not well defined [22,23,50–52]. Thus, reported values should be taken as order-of-magnitude approximation.

The momentum values are cast in terms of C_μ, $\langle C_\mu \rangle$, and $C_{\mu,\text{tot}}$ for the various Reynolds numbers surveyed in Tables 2 and 3 [22]. It should be noted that each δ_f has an optimal f_m for control ranging from 70–400 Hz, and these are not all encompassed by the data in Fig. 5. Consequently, values of J/ρ and $\langle J/\rho \rangle$ for a given modulation frequency are interpolated using an exponential fit to the three cases shown. This interpolated value is then used for expressing the momentum coefficients in Table 3 for the various optimal forcing frequencies. This interpolation is deemed appropriate based on the monotonically decreasing nature of the integral values calculated from Fig. 5, although any monotonically decreasing fitting function is likely sufficient. No such interpolation is necessary for the unmodulated data in Table 2, since the momentum production is calculated from the 100% DC profiles only.

The power dissipated by the discharge is also provided in dimensionless form as C_E, in Tables 2 and 3. The actual power for 3000 Hz actuation at 20 kV_{pp} is approximately 1.7 W/cm. For simplicity, the power dissipated by the discharge in burst mode at 50% DC is assumed to be independent of frequency and estimated as

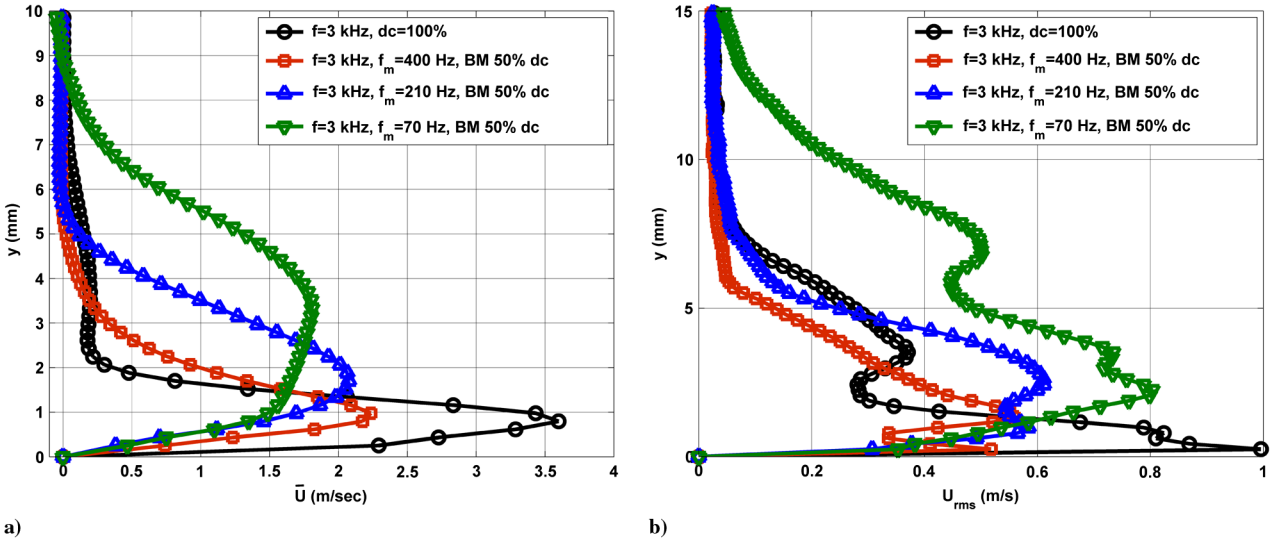

Fig. 5 Plots of a) mean and b) rms U velocity profiles for DBD plasma operating in still air at 3000 Hz carrier frequency and 20 kV_{pp} for various burst frequencies measured 20 mm downstream of electrode interface.

Table 2 Momentum and power characteristics for quasi-steady 3000 Hz actuation at 20 kV_{pp}

$Re/1000$	F_L^+	J/ρ, N/mm	$\langle J/\rho \rangle$, N/mm	C_μ, %	$\langle C_\mu \rangle$, %	$C_{\mu,\mathrm{tot}}$, %	C_E, %
240	12.7	11.8	1.3	0.041	0.005	0.046	15.6
410	7.6	11.8	1.3	0.015	0.002	0.017	3.4
750	4.2	11.8	1.3	0.005	0.001	0.006	0.6

Table 3 Momentum and power characteristics for 3000 Hz actuation at 20 kV_{pp} with various BM frequencies at DC of 50%

$Re/1000$	f_m, Hz	$F_{L,m}^+$	J/ρ, N/mm	$\langle J/\rho \rangle$, N/mm	C_μ, %	$\langle C_\mu \rangle$, %	$C_{\mu,\mathrm{tot}}$, %
				$\delta_f = 20°$			
240	120	0.5	11.9	2.3	0.042	0.008	0.050
410	210	0.5	9.3	1.3	0.012	0.002	0.014
750	400	0.5	5.6	0.7	0.002	<0.001	0.002
				$\delta_f = 30°$			
240	90	0.4	12.9	2.6	0.045	0.009	0.054
410	160	0.4	10.7	1.9	0.014	0.002	0.016
750	270	0.4	8.1	1.2	0.003	0.001	0.004
				$\delta_f = 40°$			
240	70	0.3	13.5	3.0	0.047	0.011	0.058
410	120	0.3	11.9	2.3	0.015	0.003	0.018
750	230	0.3	8.9	1.4	0.004	0.001	0.005

half the power at 100% DC for each case. Note that F^+ based on flap length (6.35 cm) is also included in Tables 2 and 3 for completeness.

Before discussing control results, some comments on the C_μ calculations are warranted. ZNMF actuation is generally characterized using only the oscillatory momentum coefficient $\langle C_\mu \rangle$, due to the periodic blowing-suction behavior. The DBD plasma actuator is certainly a ZNMF device, but the analogy with more traditional ZNMF devices such as those used by NASA is not warranted, since the plasma also produces a nonzero net mean flow [22]. Thus, the characterization of such a device is more similar to *nonzero*-net-mass-flux devices. When the wall normal plasma-induced flow is neglected as is the case here, the actuator is essentially a pulsed jet, and thus its characterization requires the inclusion of both mean and oscillatory components of momentum [15]. Despite this additional mean component, $C_{\mu,\mathrm{tot}}$ is generally an order of magnitude less than that used in NASA experiments, although it is difficult to directly compare the momentum production of these two devices. It is also important to note that values of C_μ for periodic excitation produced by piezoelectric devices in the presence of a freestream have been obtained by correlating the pressure in the actuator cavity with the velocity at the slot exit in benchtop experiments. The pressure in the actuator cavity can then be monitored during control experiments, giving a more accurate representation of the actual momentum production [11]. Calibrations for DBD plasma actuators performed using nonzero freestream have resulted in even lower estimates of momentum coefficient; thus, the values reported in Tables 2 and 3 are most likely an overestimate [53].

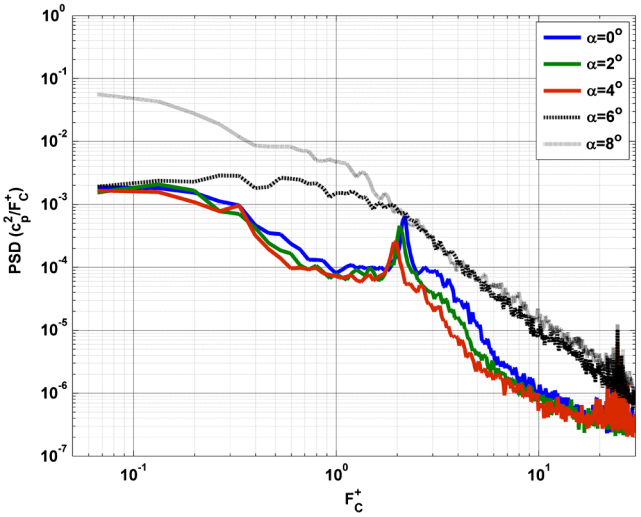

Fig. 6 Baseline PSD of fluctuating pressure measured at $x/c = 0.95$ for $Re = 410{,}000$ and $\delta_f = 20°$ at various α.

B. Baseline Verification and Characterization

Aerodynamic characteristics of the OSU version of the simplified NASA EET have been discussed previously [54,55]. In the interest of brevity, the following recounts only some of these findings relevant to the results presented in this work. The simplified NASA EET airfoil is prone to stall, due to a small radius of curvature at the LE, hence the need for the droop design in previous publications [10]. The OSU version of the NASA EET is designed without an LE droop, for simplicity, and this results in stall at relatively low α. Attempts to extend the stall angle using various tripping mechanisms were met with limited success, especially at $Re < 750{,}000$; consequently, no LE trip has been used in the results that follow. Because of these issues, results are limited to $\alpha < 6°$ for $\delta_f = 20$–$40°$ as flow separates upstream of the flap shoulder for higher α. Smaller values of δ_f are not analyzed, because separation occurs much further downstream of the flap shoulder. Despite the LE stall issues, a direct comparison of C_P and c_P for untripped OSU and NASA results shows good agreement. The flowfield over the deflected flap is characterized by vortex shedding at F_c^+ between 1–3, whereas more aggressive flap deflections give rise to lower-frequency oscillations. The dynamic signature of vortices shed from the flap shoulder obeys F^+ scaling with increasing Reynolds number and is independent of α until the separation point moves upstream. Figure 6 provides a sample of this

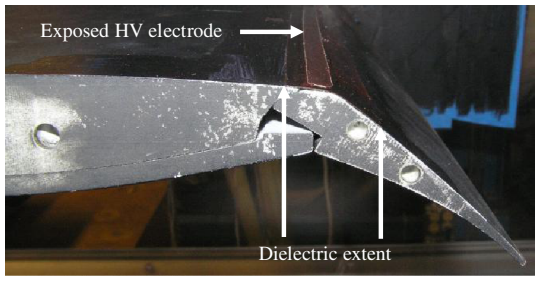

Fig. 7 Example of a DBD plasma actuator applied at the flap shoulder ($x/c \sim 0.77$) of the simplified NASA EET airfoil, $\delta_f = 30°$.

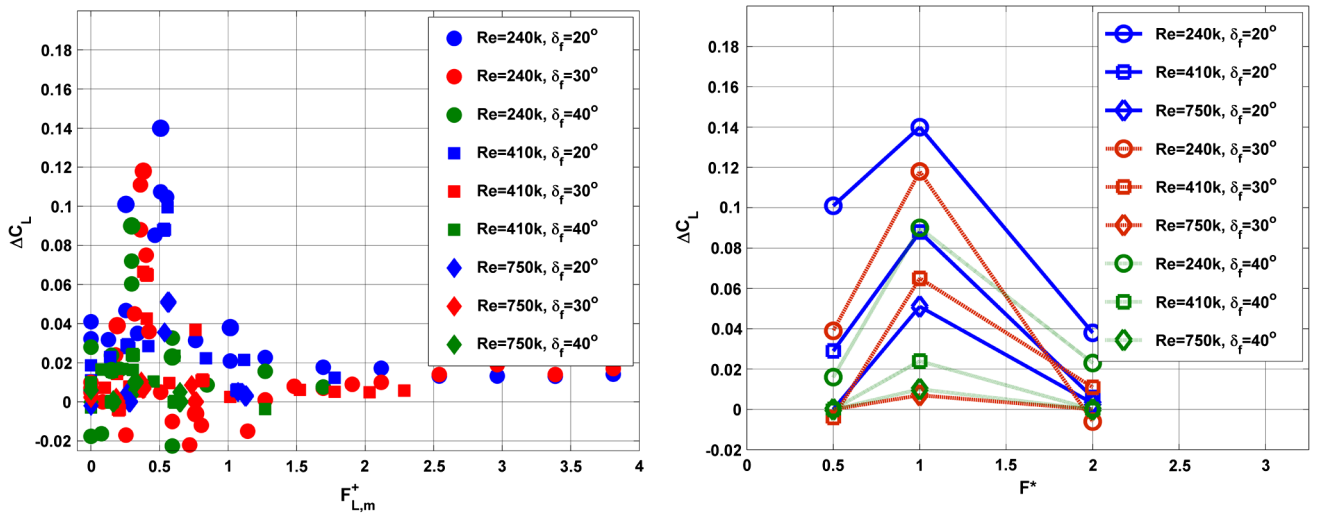

a) b)

Fig. 8 Effect of dimensionless actuation frequencies a) $F^+_{L,m}$ and b) F^* on ΔC_L at $\alpha = 0°$ for various Re and δ_f.

behavior at $Re = 410{,}000$ and $\delta_f = 20°$. These results are consistent across the test conditions previously described.

The boundary-layer velocity profile has been measured upstream of the flap shoulder using PIV at $\alpha = 0°$. In all cases, the incoming boundary layer follows a turbulent $u/U = (y/\delta)^{1/n}$ profile with n varying from 4 to 6 and ranges in thicknesses between 4.4–7.0 mm, depending on Re and δ_f. The shape factor H remains relatively constant around 1.4, ensuring that the boundary layer approaching the flap is similar in all cases [54]. The baseline results show that even though LE stall characteristics between the NASA and OSU models are different, the results are consistent at OSU prestall α, as the separating boundary layer is turbulent and has similar dynamic features upon separation.

C. Single DBD Control Results

A single DBD plasma actuator is applied to the flap shoulder near the location of maximum surface curvature as shown in Fig. 7. This is done by first deflecting the flap and then applying the various layers of adhesive tape. The resulting actuator location is $x/c \sim 0.77$, independent of δ_f. This is in contrast to the fixed actuator locations used by NASA. Thus, the most relevant comparison of forthcoming results should be made in reference to NASA actuation locations at and between FWD and slot 3, which are located at $x/c = 0.725$ and 0.757, respectively, in reference to the cruise configuration ($\delta_f = 0$) [11]. Despite the documented sensitivity of TE control authority to

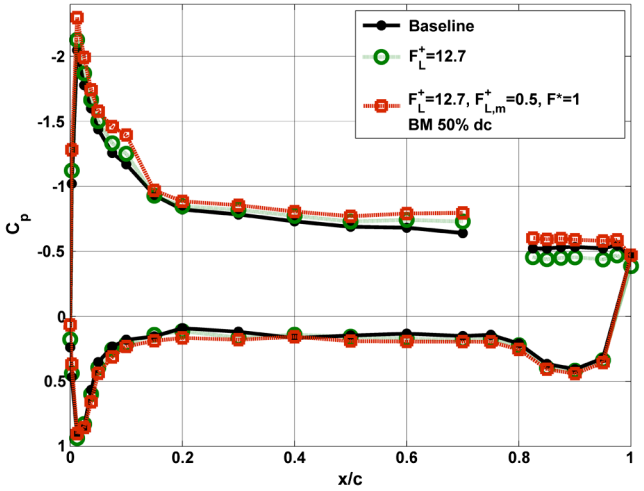

Fig. 9 Baseline and controlled C_P behavior for $Re = 240{,}000$, $\alpha = 0°$, and $\delta_f = 20°$.

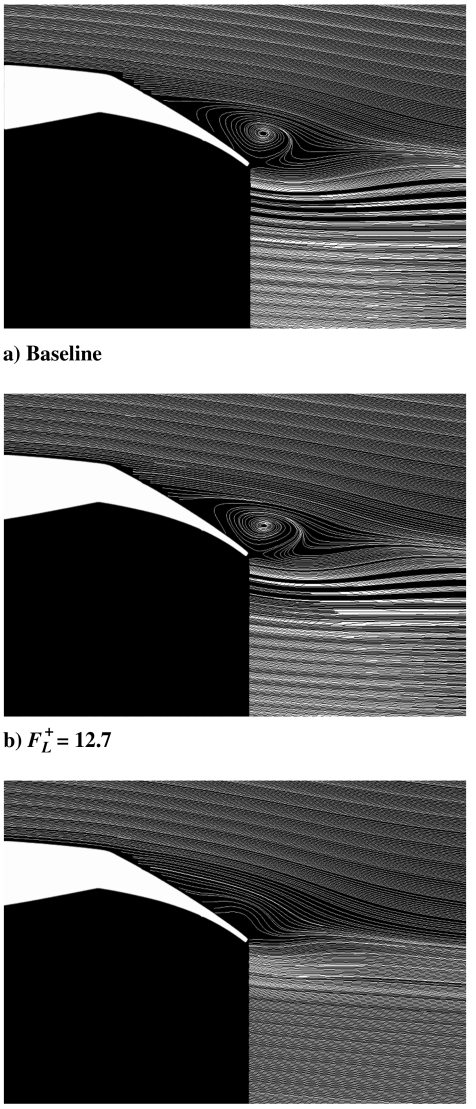

a) Baseline

b) $F^+_L = 12.7$

c) $F^+_L = 12.7$; $F^+_{L,m} = 0.5$; $F^* = 1$; BM 50% dc

Fig. 10 Baseline and controlled time-averaged streamlines for $Re = 240{,}000$, $\alpha = 0°$, and $\delta_f = 20°$.

actuator location, the following results are quite repeatable for DBD plasma actuators manually applied to the airfoil surface.

It should be noted that each time an actuator is placed on the model, the baseline flow changes slightly, due to the presence of the actuator alone: most notably, from the surface discontinuity created at the actuator leading and trailing edges. This changes the C_P profiles somewhat, but the dynamic signature of the shedding vortices remains consistent [55]. Also, the boundary layer approaching the flap is turbulent; thus, the actuator does not act as a tripping device [54]. For the remainder of the work, any reference to the baseline configuration pertains to the case, in which an actuator is present on the model surface without plasma (power off).

Results of frequency sweeps for various Reynolds numbers, δ_f, input voltages, modulation waveforms, and carrier/modulation frequencies are presented in Fig. 8a. The data are plotted against F_L^+. For the purposes of this discussion, only results outside of the ± 0.02 uncertainty/repeatability band are relevant. The actuation cases that do not employ low-frequency modulation, referred to as quasi-steady actuation hereafter, have been plotted at $F_{L,m}^+ = 0$ to reduce the abscissa range, for clarity. Only a relatively narrow band of frequencies, $F_{L,m}^+ = 0.3$–0.5, shows clear increases in C_L. In reality, this effective band of frequencies is even narrower than it appears. Portions of the data in Fig. 8a are plotted using a different scale in Fig. 8b. In this case, the modulation frequencies are normalized by f_{TE}, which is the characteristic frequency of vortex shedding from the flap (see Fig. 6 using a different F^+ length scale). A distinct frequency preference is now obvious, in that excitation at $F^* = 1$ generates the most lift enhancement. In one case, the subharmonic of this frequency ($F^* = 1/2$) also has a substantial effect, but there is no experimental evidence to suggest vortex shedding is shifted to this lower frequency. Rather, the increased C_L value seems to occur through a realizable, but less efficient amplification of the natural instability. In general, the control authority is found to decrease with increasing Re and δ_f. This frequency preference in Fig. 8 is similar to presented NASA results of lift enhancement for a slightly different version of the same airfoil using piezoelectric-driven ZNMF actuators. However, the DBD plasma actuator control authority for low-frequency excitation above $F_{L,m}^+ = 1$ and quasi-steady forcing is significantly reduced in comparison. This is due to the low-momentum nature of DBD plasma compared to the NASA actuation, which limits control authority to very narrow frequency bands, corresponding to natural flow instabilities.

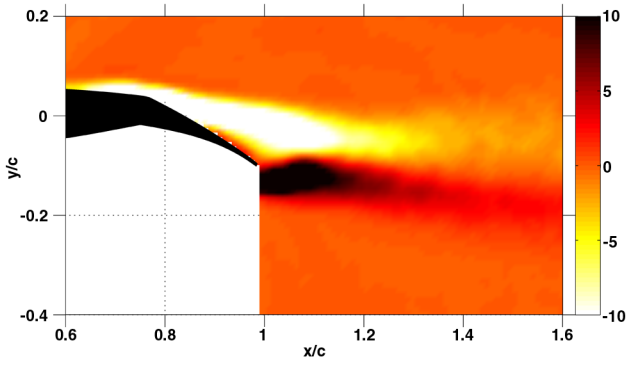

a) Baseline

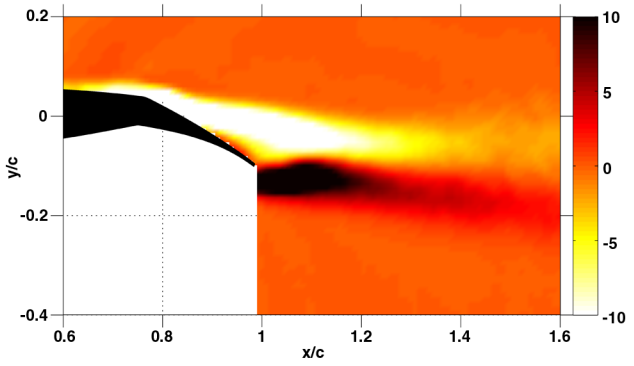

b) $F_L^+ = 12.7$

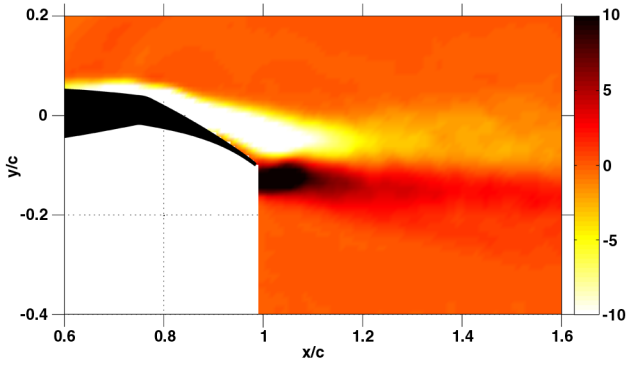

c) $F_L^+ = 12.7$; $F_{L,m}^+ = 0.5$; $F^* = 1$; BM 50% dc

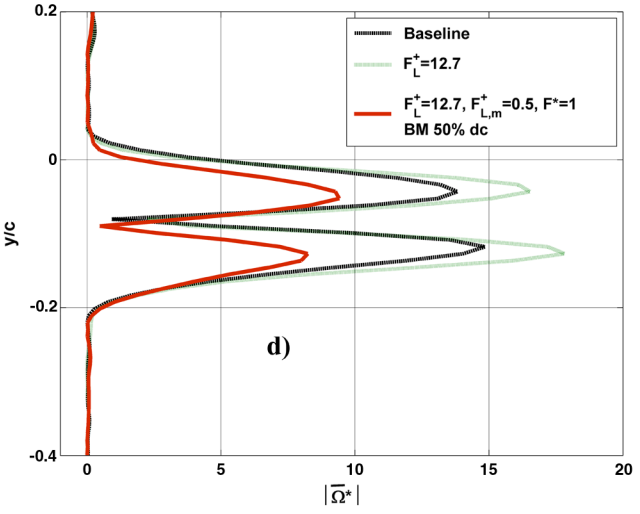

d)

Fig. 11 Plots of a–c) baseline and controlled time-averaged normalized vorticity $\bar{\Omega}^*$ for $Re = 240{,}000$, $\alpha = 0°$, and $\delta_f = 20°$ with d) profiles of vorticity magnitude at $x/c = 1.1$.

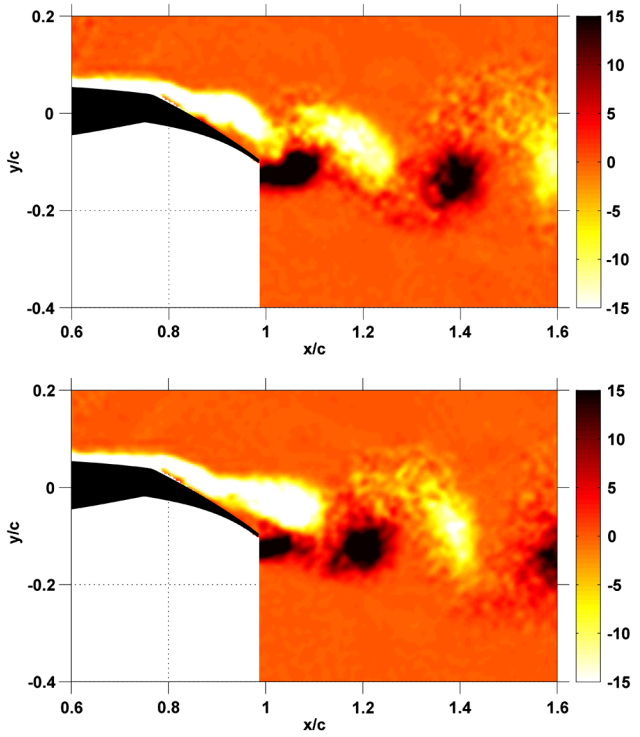

Fig. 12 Phase-averaged normalized vorticity Ω^* for $Re = 240{,}000$, $\alpha = 0°$, and $\delta_f = 20°$ forced at $F_L^+ = 12.7$, $F_{L,m}^+ = 0.5$, and $F^* = 1$ with BM at 50%. Phase difference $\Delta\Phi$ between the two frames is π.

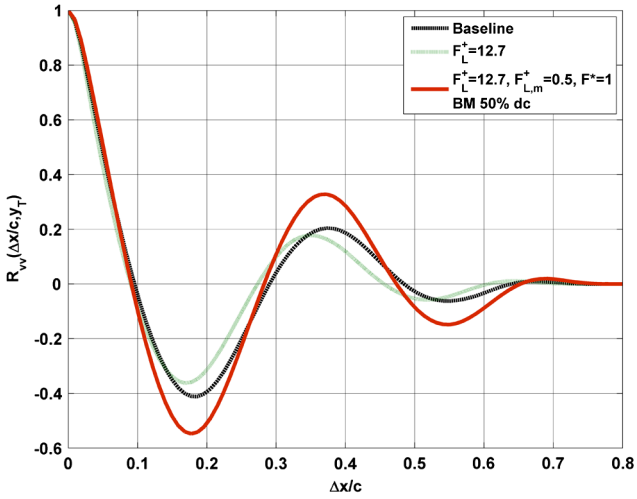

Fig. 13 Spatial correlation of the v component of velocity, R_{vv}, at $y/c = y_T$ for $Re = 240{,}000$, $\alpha = 0°$, and $\delta_f = 20°$ for baseline and controlled flows.

A sample set of C_P curves for the results of Fig. 8 are presented in Fig. 9. The gap in the C_p curves over the flap shoulder corresponds to the surface of the model covered by the actuator, which prevents static pressure measurements. The difference between the baseline and both actuation cases is clearly visible on the flap, due to changing characteristics of the near wake (see Fig. 10). The quasi-steady actuation case at $F_L^+ = 12.7$ generates less suction on the flap while accelerating the flow at the LE and upstream of the flap shoulder, consistent with circulation increase due to a slight delay in separation. Forcing at $F^* = 1$ increases suction on the flap and further enhances circulation around the entire model. This is indicated by even greater flow acceleration at the LE and flap shoulder in comparison to the quasi-steady case. This circulation increase and corresponding upstream effect create the majority of the measured lift enhancement. This behavior is typical of TE airfoil separation control, in that a significant portion of the lift enhancement is due to upstream effects, rather than full reattachment of flow to the flap [3,11]. It should also be noted that the model scale and obstruction of static pressure taps by the actuator do not allow the resolution of any suction peak near the flap shoulder as exhibited in NASA results [9,11,12]. However, a slight favorable pressure gradient is visible around $x/c = 0.7$ for both forcing cases, suggesting that it does exist. It should be noted that effective control near the flap shoulder can result in a local suction peak with similar strength to that observed at the LE at low α [12]. The lack of C_P resolution here implies that the presented ΔC_L values are an underestimate.

Figure 10 provides a more illustrative example of the TE behavior exhibited in the C_P curves. The streamlines calculated from two-component PIV are shown for the three cases in Fig. 9. The effect of actuation is readily apparent on the time-averaged flowfield. Quasi-steady forcing at $F_L^+ = 12.7$ (Fig. 10b) serves to energize the

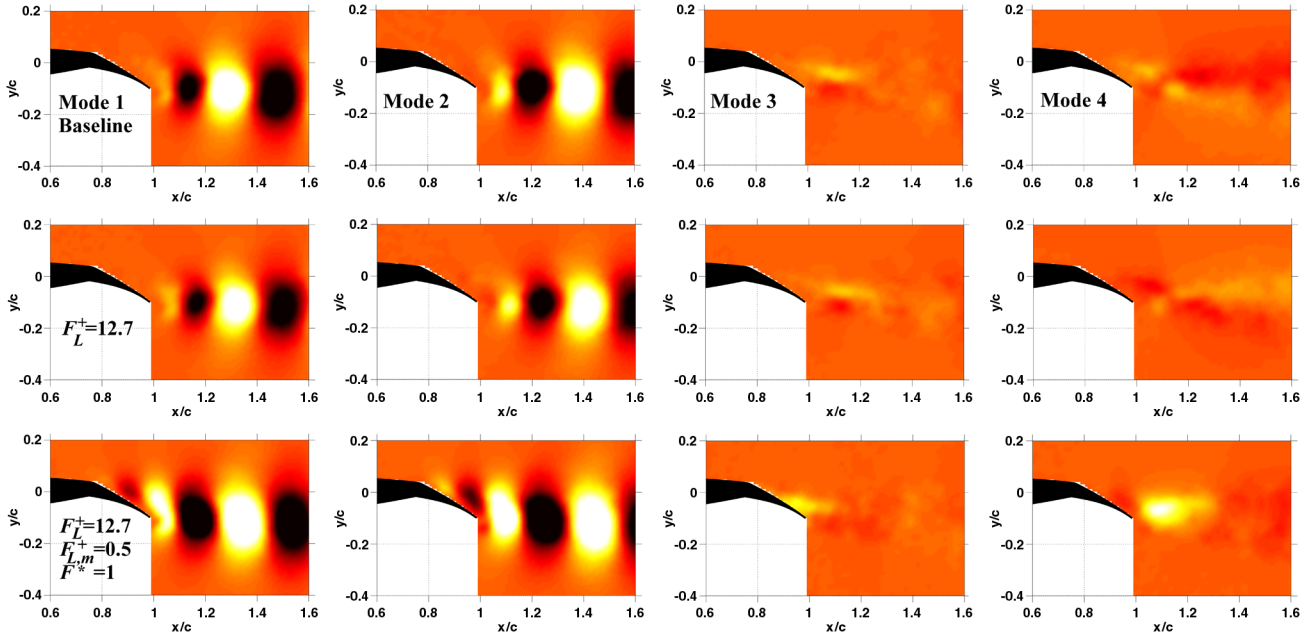

Fig. 14 First four baseline and controlled POD modes of the v component of velocity for $Re = 240{,}000$, $\alpha = 0°$, and $\delta_f = 20°$ using BM with 50% DC when applicable (third row).

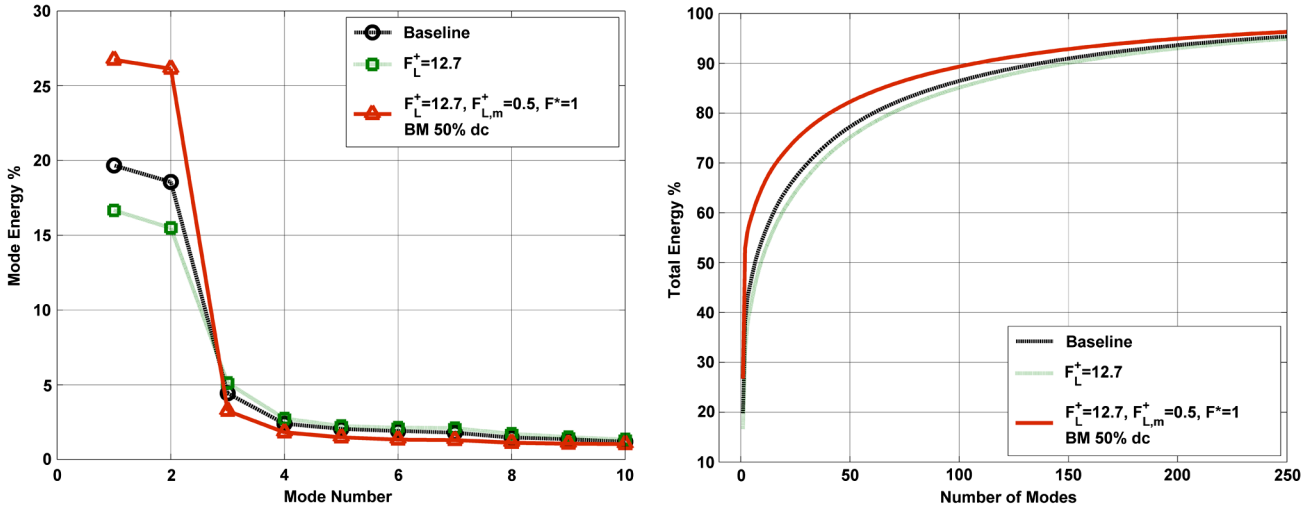

a) b)

Fig. 15 Plots of a) modal energy and b) cumulative energy for baseline and controlled POD modes for $Re = 240{,}000$, $\alpha = 0°$, and $\delta_f = 20°$.

boundary layer and move the separation point downstream. This delayed separation has the effect of lengthening and slightly narrowing the recirculation region near the flap, creating the higher C_P value shown in Fig. 9. This also confirms the suggestion that a slightly stronger suction peak should exist in the C_P curve near the flap shoulder in comparison to the baseline. The persistence of the recirculation region on the flap explains the diminished circulation increase in comparison to forcing at $F^* = 1$ (Fig. 10c), which has a drastic effect on the time-averaged streamlines. In this case, the separation location has again moved downstream, but the streamlines resemble almost potential flow with only a slight recirculation region visible. This also confirms the existence of a stronger suction peak near the flap shoulder in comparison to both the baseline and quasi-steady forcing cases. Thus, the effect of unsteady plasma actuation is not limited to a local delay in separation, but has the additional benefit of enhancing freestream momentum transfer to the wake, even after separation ensues, which further augments circulation.

The time-averaged spanwise vorticity fields corresponding to the streamlines of Fig. 10 are shown in Fig. 11. As expected, strong regions of vorticity exist above and below the flap, corresponding to the shear layer between the high-speed freestream and recirculation region. Strong vorticity on the flap persists for all cases, emphasizing that even when time-averaged streamlines more closely follow the flap surface as in Fig. 10c, there is still considerable interaction here from flow structures excited by the plasma (Fig. 11c). This is further discussed in the context of phase-averaged measurements that follow (Fig. 12). The vorticity fields additionally highlight the extent of recirculation region and its effect on the time-averaged wake. As previously shown for $\delta_f = 30°$ with an actuator less optimized for inducing velocity [54], quasi-steady forcing serves to delay separation, but lengthens the extent of the recirculation region in comparison to both the baseline and $F^* = 1$ forcing cases. The latter case is found to reduce the size of the recirculation region and pull the region of strong vorticity closer to the flap element. These effects are visible in the vorticity on both the pressure and suction sides of the airfoil downstream of the flap and are most evident from profiles at $x/c = 1.1$ (Fig. 11d).

The time-averaged results of Figs. 10 and 11 do not truly represent the physical behavior of the flow. Recall that the most striking benefits of control are realized by amplifying the natural instability of the TE flowfield. In a temporal sense, this slightly delays boundary-layer separation, but a more obvious result is the amplification and organization of the natural vortex shedding. This increases entrainment of freestream momentum into the shear layer and recirculating region, even beyond the point of separation from the flap surface. While this does not serve to fully reattach the flow, the reduced size of the recirculating region has a profound effect on the circulation around the model and subsequently on the sectional C_L, as shown in Figs. 8 and 9. The organized nature of vortex shedding is most apparent from measurements of phase-locked vorticity (Fig. 12). This also highlights a detrimental aspect of forcing at $F^* = 1$, in that the dynamic loads on the flap due to vortex shedding are substantially increased [47]. In some cases, this can result in oscillatory aerodynamic forces [56], although this has not been observed in our work. It should be noted that it is not possible to shift this oscillation frequency away from f_{TE} by more than a few hertz, due to the low-momentum production of the DBD plasma actuator used in this work.

Spatial correlation of PIV data is used to investigate the frequency content in the wake in Fig. 13. Pressure spectra were previously employed, but transducers have subsequently been damaged by the plasma discharge and these measurements are no longer possible. Since the frequency content of the baseline flow is known from previous characterization, one can directly correlate the spatial velocity fluctuations in the wake to temporal fluctuations of pressure. The normalized spatial correlation of the fluctuating vertical component of velocity, R_{vv},

$$R_{vv}(\Delta x, y_T) = \frac{\int_{-\infty}^{\infty} v(x, y_T) v(x + \Delta x, y_T)\, dx}{\int_{-\infty}^{\infty} [v(x, y_T)]^2\, dx}$$

is computed along the y/c coordinate associated with the trailing edge of the deflected flap ($y/c = y_T$). This location is a reasonable estimate of the symmetry plane associated with the spatial dynamics

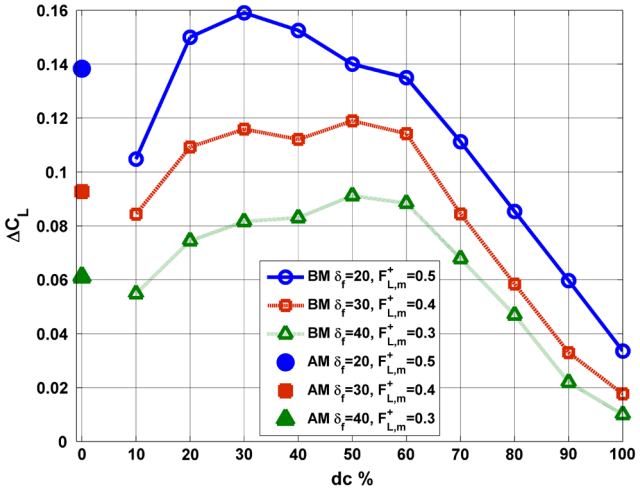

Fig. 16 Effect of modulation waveform on ΔC_L for $Re = 240{,}000$ and $\alpha = 0°$ and variable δ_f when forcing at $F_L^+ = 12.7$, $F^* = 1$.

of the vertical fluctuating velocity component in the turbulent wake (see Fig. 14). A correlation function is computed for each instantaneous fluctuating vertical velocity field and the average correlation waveform is computed using the 1000-image sample set. The baseline and $F^* = 1$ forcing cases exhibit a similar wavelength, with the latter being amplified considerably due to forcing near the natural vortex-shedding frequency. The quasi-steady forcing case has slightly weaker correlation levels than the baseline, but at a shorter wavelength, consistent with oscillations at a higher frequency. While this shift in the correlation peak toward higher frequencies is weak, the trend is in general agreement with pressure spectra of NASA using piezoelectric ZNMF actuation at high frequency ($F_L^+ \sim 13$) [11]. This suggests that despite the ZNMF pulsed-blowing-like behavior of DBD plasma high-frequency excitation, the flow response is quite similar to that observed for more conventional ZNMF actuators.

The proper orthogonal decomposition (POD) method is used to gain additional insight into the dominant characteristics of the flowfield [57]. The first four POD modes for the v component of velocity for the baseline and controlled flows using quasi-steady ($F_L^+ = 12.7$) and $F^* = 1$ forcing are shown in Fig. 14. In all cases, a distinct well-organized spatial mode pattern indicative of oscillations exists in the trailing-edge wake. This is expected for the baseline and low-frequency ($F^* = 1$) forcing case and further supports the suggestion that oscillations persist near the natural shedding frequency even for quasi-steady forcing, although the shorter wavelength is not readily apparent here. Forcing at $F^* = 1$ shows more amplified spatial modes compared to the baseline and quasi-steady cases and a recognizable signature of structures emanating from the flap shoulder near the actuator location. Note that previous analysis of similar data when forcing at $F^* = 2$ showed very-low-energy spatial modes, consistent with excitation at the first harmonic of the natural shedding, but these had little effect on the overall flowfield [58].

Figure 15a presents corresponding energy results for the data of Fig. 14 and further emphasizes the low-dimensional organized nature of the unsteady forced flowfield ($F^* = 1$) as over 50% of the total kinetic energy is contained in modes 1 and 2. This number approaches 40%, even for the baseline case. The quasi-steady forcing ($F_L^+ = 12.7$) removes energy from the first two modes and gives it to mode 3, in particular. Figure 15b shows cumulative energy of the data of Fig. 15a, in which it is shown that the increased energy in modes 1 and 2 for the low-frequency-forcing case accelerates convergence significantly, while the quasi-steady forcing is actually decelerated below the baseline. The strong low-dimensional behavior emphasizes how challenging it is to force the flow away from this coherent state, especially with a low-momentum actuator.

The previous results have focused on modulation of the high-frequency plasma-carrier waveform using BM at 50% duty cycle. This is a typical modulation strategy for DBD plasma; however, the use of amplitude modulation (AM) is often employed for other flow control actuators [9,59]. Examples of these modulation waveforms are shown in Fig. 2. NASA showed that modulating the high-frequency waveform using BM, rather than AM, further increases the efficiency of actuation, since the DC can be lowered, thereby

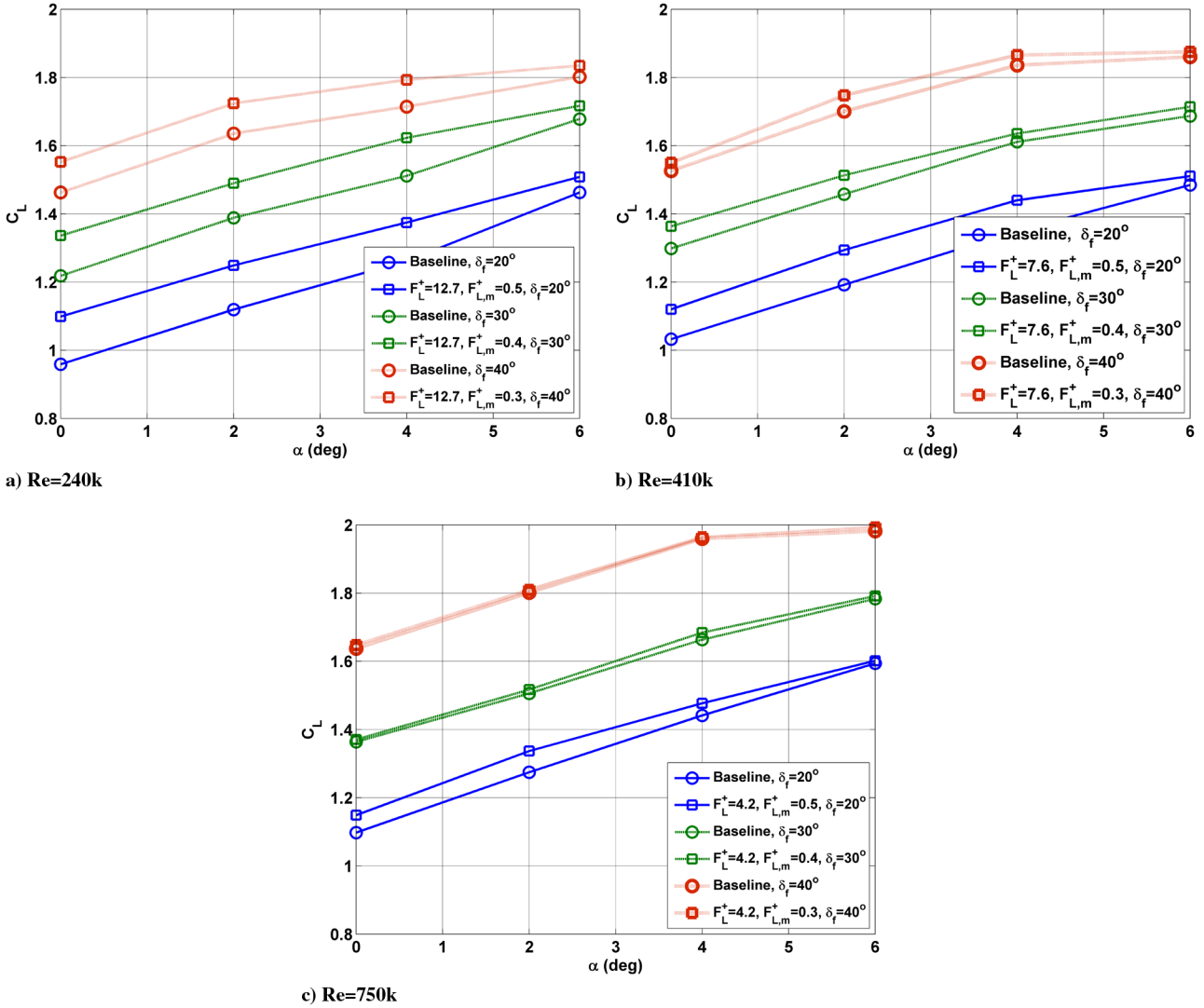

a) Re=240k

b) Re=410k

c) Re=750k

Fig. 17 Effect of Re, α, and δ_f on ΔC_L for forcing at $F^* = 1$ using BM with 50% DC.

decreasing power consumption [9]. A similar study for three δ_f at $Re = 240,000$ is shown in Fig. 16 using DBD plasma. As a point of reference, the power consumption of AM is approximately equal to BM at 40% DC in this work [47,55]. The progressively more challenging nature of controlling separation as δ_f increases is quite apparent from this data. There is a clear duty-cycle effect, as values of at least 20% represent a significant improvement over the lower case (DC of 10%) and each flap configuration has a preferred range of DC for control that increases with δ_f. Beyond this effective range, the control authority decays linearly with duty cycle. Previous work has discussed this phenomenon and the effect of the carrier and modulation signal [47]. Note that studies of LE separation control with DBD plasma actuators report significant control authority and even complete reattachment for duty cycles as low as 6% [60]. The results of Fig. 16 highlight the more challenging problem of separation control over a TE flap, which requires greater periodic momentum input in comparison [11].

The results of Fig. 16 show that BM can be both more efficient and more effective than AM for enhancing lift, depending on the DC employed. Recent publications using time-resolved velocity measurements in still air qualitatively explain this behavior [61,62]. Each low-frequency high-voltage plasma burst creates a velocity pulse that roughly mimics a first-order response on which is superimposed a high-frequency oscillation corresponding to the plasma-carrier frequency. The corresponding velocity decay between bursts is also exponential with time. Referring to Fig. 16, at low duty cycles (10%), the velocity may never reach its peak steady-state value, thereby limiting control authority. Similarly, at high duty cycles (90%), sufficient flow relaxation time may not be present to generate the perturbation effect necessary for control. This has also been explored for AM waveforms with similar results [62]. In this case, both voltage-on and voltage-off transients may play a role. While these recent publications provide a qualitative explanation of the behavior, the effect of carrier frequency, modulation frequency, and, perhaps most important, freestream velocity must be considered to fully quantify this behavior.

The data of Fig. 16 generally agree with NASA results, but the functional relationship between ΔC_L and DC is quite different [9]. In NASA work, ΔC_L saturates at DC of 45% for $\delta_f = 20°$ at $\alpha = 6°$ with excitation near the flap shoulder. Further increases in DC required more power input, but showed none of the degrading effects on C_L exhibited here. Also, the BM cases for NASA were found to be more efficient, but not more effective than AM. These discrepancies are likely due to the pulsed-blowing nature of the DBD plasma actuator compared to pulsed blowing/suction in the NASA case and the DBD induced flow transient behavior mentioned above.

The efficacy of DBD plasma actuators for TE separation control at nonzero α is shown in Fig. 17. Recall that the dynamics of the TE flowfield remain relatively consistent as long as the separation location does not change (Fig. 6). This is also apparent in control results, as forcing at $F^* = 1$ for a given δ_f creates a near-constant increase in C_L for $\alpha < 6°$. The diminished control authority at $\alpha = 6°$ is due to the movement of the separation point upstream of the actuation location, which is supported by existing literature [12,41].

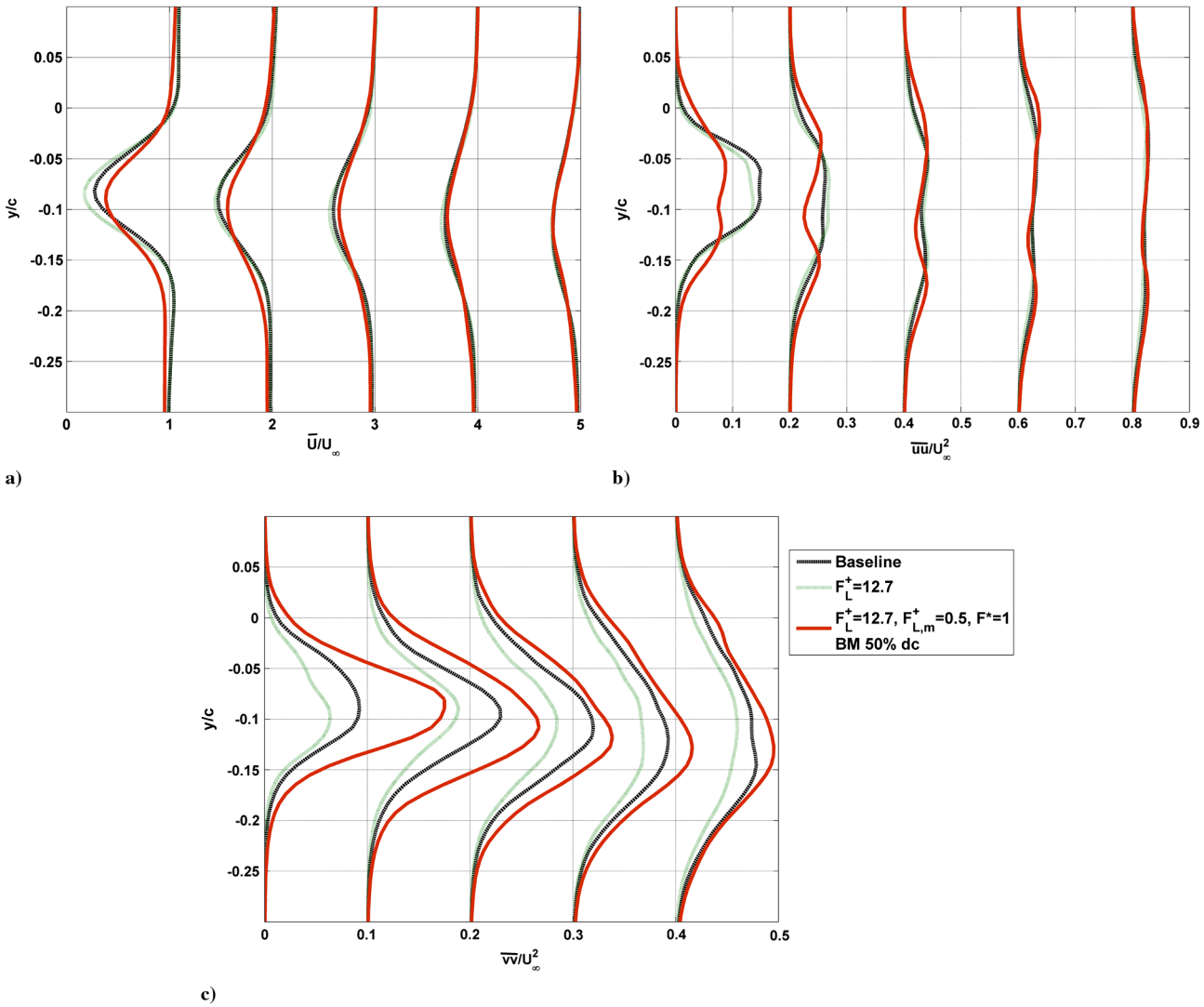

Fig. 18 Plots of a) baseline and controlled normalized $\bar{U}$ velocity profiles and Reynolds normal stresses b) $\overline{uu}$ and c) $\overline{vv}$ for $Re = 240,000$, $\alpha = 0$, and $\delta_f = 20$ at $x/c = 1.1$, 1.2, 1.3, 1.4, and 1.5 (left to right and offset for clarity).

To retain the benefits of AFC at the flap shoulder at $\alpha \geq 6°$, some PFC or AFC is required at the LE to maintain attached flow along the main element up to the flap shoulder. This simultaneous use of the LE and TE actuation can further increase airfoil performance [9,11,12].

As expected, the control authority decreases with increasing δ_f and Reynolds number. In the former, the progressively more severe adverse pressure gradient and surface curvature along the flap shoulder requires greater momentum input to delay separation and enhance circulation around the model. The reduction in actuator control authority as Reynolds number is increased (in this case, by increasing U_∞) is captured by C_μ and is well established in the literature for both DBD plasma and more traditional ZNMF devices operating at a fixed amplitude [11,12,22].

The effect of control on C_D has yet to be considered. NASA results show that forcing can have a significant effect on C_{dp} that is strongly dependent on both C_μ and actuation location and does not necessarily correlate with C_L [9,11,12]. Because of the inaccuracy of C_{dp} for quantifying total drag values and the obstruction of static pressure taps by the plasma actuator, these effects are not considered. Instead, calculations of C_D from PIV wake surveys that include contributions of turbulent stresses are employed using

$$C_D = 2\int_{-0.3}^{.1} \frac{\bar{U}}{U_\infty}\left(1 - \frac{\bar{U}}{U_\infty}\right) d\left(\frac{y}{c}\right) + \int_{-0.3}^{.1} \left(\frac{\overline{vv} - \overline{uu}}{U_\infty^2}\right) d\left(\frac{y}{c}\right)$$

where $\bar{U}$ and U_∞ are the time-averaged local and freestream velocity, respectively [63]. Profiles of the three relevant parameters in this expression are shown in Fig. 18. The effect of control is apparent in the near-wake velocity profiles, but this disappears downstream (Fig. 18a). Note that the profiles are offset for clarity and the spanwise Reynolds number normal stress is assumed to be negligible. The $\overline{uu}$ stress behaves similarly to the mean velocity, in that the effects of control are seen in the near wake, but also quickly dissipate downstream (Fig. 18b). Only the $\overline{vv}$ stress shows a persistent effect of control (Fig. 18c). This is expected, given the influence of coherent spanwise vortices on this component of the Reynolds stress tensor. The above profile suggests that C_D should increase for $F^* = 1$ forcing. While this seems apparent in the wake profiles, the contribution of this term to the C_D calculation is quite small, less than 10% on average across the Reynolds number and δ_f parameter space, such that overall calculations of C_D at $x/c > 1.4$ show no significant change between the baseline and control cases at $\alpha = 0°$, due to slight variations in the $\bar{U}$ and $\overline{uu}$ profiles. The uncertainty surrounding C_D calculations from wake surveys for these separated flows is well established [64]. Thus, significantly more work is required to quantify the effects of DBD plasma on C_D in this flowfield, but at present, increasing C_L via instability amplification does not appear to be prohibitive from a drag perspective.

D. Perspective on SDBD Control Results

As the NASA and ADVINT programs have shown, increasing the amplitude of forcing generally serves to improve control authority until some saturation level is reached. The scaling laws for this behavior are not well defined and an open question is whether to cast this in terms of C_μ, velocity ratio, etc. [14]. In this work, the amplitude effect has been cast as C_μ and values are generally one order of magnitude less than those used by NASA. Yet control results at low Reynolds numbers are comparable when forcing at $F^* = 1$ seemingly rendering DBD plasma quite efficient from a C_μ standpoint when used primarily to amplify the natural instability. This analysis is complicated by the vague definition of C_μ calculations for DBD plasmas as well as the uncertainty on both the effects of direction and surface area/volume over which control is applied, which prevents a direct comparison to more conventional ZNMF actuators. It should be noted that a complete optimization for DBD plasma-induced flow has not been employed in this work, and significant improvements have been demonstrated in the literature. Recent studies that show plasma-induced thrust can be increased by an order of magnitude suggest that application of these devices at more practical takeoff and landing velocities is realizable [25]. An open question is whether additional increases in C_μ from DBD plasma follow trends similar to those shown for C_μ increases in the ZNMF NASA work [9,11,12]. Investigation of this possibility requires more robust dielectrics that are integrated into the airfoil with higher-voltage excitation.

V. Conclusions

Control of turbulent boundary-layer separation over the TE flap of a high-lift airfoil has been demonstrated using a single DBD plasma actuator placed near the flap shoulder. The actuator is mounted across the span of the airfoil near the region of maximum curvature of the flap shoulder to produce nominally two-dimensional perturbations in the streamwise direction. Quasi-steady forcing delays separation and increases C_P on the flap, due to a lengthening and slight thinning of the separated region, but does not have a drastic effect on the measured lift. Amplifying the natural instability associated with vortex shedding from the flap shoulder by forcing with low-frequency modulated versions of the high-frequency waveform is most effective for increasing lift and reducing the time-averaged recirculation region on the flap. This results in increased dynamic loading and more organized turbulent fluctuations in the wake. Amplification of this natural instability generates more negative C_P values on the flap, but the majority of the measured lift increase is due to upstream effects from enhanced circulation around the entire model. These results persist even when drastic separation delay is not achieved at high δ_f. The C_L increase due to amplification of the natural instability is relatively independent of α as long as the separation location and the underlying dynamics (i.e., vortex-shedding frequency) do not change. The control authority of the actuator generally decreases with increasing Re and δ_f for actuators operating at fixed amplitude, consistent with the limited nature of DBD plasma momentum addition.

Both the effectiveness and efficiency of the actuator for forcing at low frequencies can be enhanced using a square-wave modulation signal (BM) instead of a sinusoidal signal (AM). Recent publications suggest that this is due to transient effects of the plasma-induced flow when produced with low-frequency modulation [61,62]. Each δ_f is found to have a preferred duty-cycle range for BM that increases with increasing δ_f. Beyond this preferred duty cycle, control authority is found to decrease considerably. The falloff at high DC is believed to be due to the ZNMF pulsed-blowing nature of the DBD plasma actuator and is in contrast to existing data for a similar airfoil using more traditional piezoelectric ZNMF excitation [9].

The findings, aside from the DC effect, are generally consistent with a similar study by NASA using piezoelectric-driven ZNMF actuators on a larger-scale version of the same airfoil. Still-air actuator characterization shows that values of C_μ for DBD plasma on the airfoil are generally an order of magnitude lower than those used at NASA, yet control authority, especially at low Reynolds numbers, is comparable. The difficulty associated with a direct comparison between these two types of actuators is admitted. However, these results suggest two obvious questions: Do further increases in C_μ generate a trend similar to that shown by NASA? Is DBD plasma as efficient from a momentum perspective for amplifying instabilities in this flowfield as C_μ appears to show? Definitive answers require future work, but such studies are certainly warranted, given recent advances in DBD plasma thrust generation that may make their use in transport aircraft feasible.

Acknowledgments

This work is supported by the U.S. Air Force Research Laboratory, Dayton Area Graduate Studies Institute Student-Faculty Graduate Fellowship, and the Howard D. Winbigler Professorship at the Ohio State University. The authors would like to thank Igor Adamovich, Kristine McElligott, Munetake Nishihara, Chris Rethmel, and Keisuke Takashima for assistance with the actuation system, experimental setup, and figures.

References

[1] McLean, J., Crouch, J., Stoner, R., Sakurai, S., Seidel, G., Feifel, W., and Rush, H., "Study of the Application of Separation Control by Unsteady Excitation to Civil Transport Aircraft," NASA CR-1999-209338, 1999.

[2] Smith, D., Dickey, E., and Klein, T. V., "The ADVINT Program," AIAA Paper 2006-2854, 2006.

[3] Kiedaisch, J., Nagib, H., and Demanett, B., "Active Flow Control Applied to High-Lift Airfoils Utilizing Simple Flaps," AIAA Paper 2006-2856, 2006.

[4] Nagib, H., Kiedaisch, J., Reinhard, P., and Demanett, B., "Control Techniques for Flows with Large Separated Regions: A New Look at Scaling Parameters," AIAA Paper 2006-2857, 2006.

[5] Nagib, H., Kiedaisch, J., Reinhard, P., and Demanett, B., "Active Flow Control for High Lift Airfoils: Separation versus Circulation Control," AIAA Paper 2007-1119, 2007.

[6] Kiedaisch, J., Demanett, B., Reinhard, P., and Nagib, H., "Active Flow Control for High Lift Airfoils: Dynamic Flap Actuation," AIAA Paper 2007-1120, 2007.

[7] DeSalvo, M., Whalen, E., and Glezer, A., "High-Lift Enhancement Using Fluidic Actuation," AIAA Paper 2010-0863, 2010.

[8] Melton, L., Yao, C.-S., and Seifert, A., "Active Control of Separation from the Flap of a Supercritical Airfoil," AIAA Paper 2003-4005, 2003.

[9] Melton, L., Yao, C.-S., and Seifert, A., "Application of Excitation from Multiple Locations on a Simplified High-Lift System," AIAA Paper 2004-2324, 2004.

[10] Melton, L., Schaeffler, N., Yao, C.-S., and Seifert, A., "Active Control of Flow Separation from Supercritical Airfoil Leading-Edge Flap Shoulder," *Journal of Aircraft*, Vol. 42, No. 5, 2005, pp. 1142–1149. doi:10.2514/1.10294

[11] Melton, L., Yao, C.-S., and Seifert, A., "Active Control of Separation from the Flap of a Supercritical Airfoil," *AIAA Journal*, Vol. 44, No. 1, 2006, pp. 34–41. doi:10.2514/1.12225

[12] Melton, L., Schaeffler, N., and Lin, J., "High-Lift System for a Supercritical Airfoil: Simplified by Active Flow Control," AIAA Paper 2007-0707, 2007.

[13] Pack, L. G., Schaeffler, N. W., Yao., C. S., and Seifert, A., "Active Control of Separation from the Slat Shoulder of a Supercritical Airfoil," AIAA Paper 2002-3156, 2002.

[14] Seifert, A., and Tillman, C., "Fixed Wing Airfoil Applications," *Fundamentals and Applications of Modern Flow Control*, edited by R. Joslin, and D. Miller, Vol. 231, Progress in Astronautics and Aeronautics, AIAA, Reston, VA, 2009, pp. 231–257.

[15] Greenblatt, D., and Wygnanski, I., "The Control of Flow Separation by Periodic Excitation," *Progress in Aerospace Sciences*, Vol. 36, 2000, pp. 487–545. doi:10.1016/S0376-0421(00)00008-7

[16] Seifert, A., Darabi, A., and Wygnanski, I., "Delay of Airfoil Stall by Periodic Excitation," *Journal of Aircraft*, Vol. 33, No. 4, 1996, pp. 691–698. doi:10.2514/3.47003

[17] Darabi, A., and Wygnanski, I., "Active Management of Naturally Separated Flow over a Solid Surface. Part 1. The Forced Reattachment Process," *Journal of Fluid Mechanics*, Vol. 510, 2004, pp. 105–129. doi:10.1017/S0022112004009231

[18] Cerchie, D., Halfron, E., Hammerich, A., Han, G., Taubert, L., Trouve, L., Varghese, P., and Wygnanski, I., "Some Circulation and Separation Control Experiments," *Applications of Circulation Control Technology*, edited by R. Joslin, and G. Jones, Vol. 214, Progress in Astronautics and Aeronautics, AIAA, Reston, VA, 2006, pp. 113–165.

[19] Seifert, A., and Pack, L., "Active Flow Separation Control on Wall-Mounted Hump at High Reynolds Numbers," *AIAA Journal*, Vol. 40, No. 7, 2002, pp. 1363–1372. doi:10.2514/2.1796

[20] Moreau, E., "Airflow Control by Non-Thermal Plasma Actuators," *Journal of Physics D: Applied Physics*, Vol. 40, 2007, pp. 605–636. doi:10.1088/0022-3727/40/3/S01

[21] Corke, T., Post, M., and Orlov, D., "Single Dielectric Barrier Discharge Plasma Enhanced Aerodynamics: Physics, Modeling and Applications," *Experiments in Fluids*, Vol. 46, 2009, pp. 1–26. doi:10.1007/s00348-008-0582-5

[22] Greenblatt, D., Goksel, B., Rechenberg, I., Schule, C., Romann, D., and Paschereit, C., "Dielectric Barrier Discharge Flow Control at Very Low Flight Reynolds Numbers," *AIAA Journal*, Vol. 46, No. 6, 2008, pp. 1528–1541. doi:10.2514/1.33388

[23] Mabe, J., Calkins, F., Wesley, B., Woszidlo, R., Taubert, L., and Wygnanski, I., "Single Dielectric Barrier Discharge Plasma Actuators for Improved Airfoil Performance," *Journal of Aircraft*, Vol. 46, No. 3, 2009, pp. 847–855. doi:10.2514/1.37638

[24] Poggie, J., Tillman, C., Flick, P., Silkey, J., Osborne, B., Ervin, G., Maric, D., Mangalam, S., and Mangalam, A., "Closed-Loop Stall Control on a Morphing Airfoil Using Hot-Film Sensors and DBD Actuators," AIAA Paper 2010-0547, 2010.

[25] Thomas, F., Corke, T., Igbal, M., Kozlov, A., and Schatzman, D., "Optimization of Dielectric Barrier Discharge Plasma Actuators for Active Aerodynamic Flow Control," *AIAA Journal*, Vol. 47, No. 9, 2009, pp. 2169–2178. doi:10.2514/1.41588

[26] Opaits, D., Likhanskii, A., Neretti, G., Zaidi, S., Shneider, M., Miles, R., and Macheret, S., "Experimental Investigation of Dielectric Barrier Discharge Plasma Actuators driven by Repetitive High-Voltage Nanosecond Pulses with DC or Low Frequency Sinusoidal Bias," *Journal of Applied Physics*, Vol. 104, 2008, Paper 043304. doi:10.1063/1.2968251

[27] Little, J., Takashima, K., Nishihara, M., Adamovich, I., and Samimy, M., "High Lift Airfoil Leading Edge Separation Control with Nanosecond Pulse Driven DBD Plasma Actuators," AIAA Paper 2010-4256, 2010.

[28] Roupassov, D., Nikipelov, A., Nudnova, M., and Starikovskii, A., "Flow Separation Control by Plasma Actuator with Nanosecond Pulsed-Periodic Discharge," *AIAA Journal*, Vol. 47, No. 1, 2009, pp. 168–185. doi:10.2514/1.38113

[29] Samimy, M., Kim, J.-H., Kastner, J., Adamovich, I., and Utkin, Y., "Active Control of High-Speed and High-Reynolds-Number Jets Using Plasma Actuators," *Journal of Fluid Mechanics*, Vol. 578, 2007, pp. 305–330. doi:10.1017/S0022112007004867

[30] Forte, M., Jolibois, J., Pons, J., Moreau, E., Touchard, G., and Cazalens, M., "Optimization of a Dielectric Barrier Discharge Actuator by Stationary and Non-Stationary Measurements of the Induced Flow Velocity: Application to Airflow Control," *Experiments in Fluids*, Vol. 43, 2007, pp. 917–928. doi:10.1007/s00348-007-0362-7

[31] Enloe, C., McHarg, M., and McLaughlin, T., "Time-Correlated Force Production Measurements of the Dielectric Barrier Discharge Plasma Aerodynamic Actuator," *Journal of Applied Physics*, Vol. 103, 2008, Paper 073302. doi:10.1063/1.2896590

[32] Kim, W., Do, H., Mungal, G., and Cappelli, M., "On the Role of Oxygen in Dielectric Barrier Discharge Actuation of Aerodynamic Flows," *Applied Physics Letters*, Vol. 91, 2007, Paper181501. doi:10.1063/1.2803755

[33] Font, G., Enloe, C., Newcomb, J., Teague, A., Vasso, A., and McLaughlin, T., "Effects of Oxygen Content on the Behavior of the Dielectric Barrier Discharge Aerodynamic Plasma Actuator," AIAA Paper 2010-0545, 2010.

[34] Huang, J., Corke, T., and Thomas, F., "Plasma Actuators for Separation Control of Low-Pressure Turbine Blades," *AIAA Journal*, Vol. 44, No. 1, 2006, pp. 51–57. doi:10.2514/1.2903

[35] Patel, M., Ng, T., Vasudevan, S., Corke, T., Post, M., McLaughlin, T., and Suchomel, C., "Scaling Effects of an Aerodynamic Plasma Actuator," *Journal of Aircraft*, Vol. 45, No. 1, 2008, pp. 223–236. doi:10.2514/1.31830

[36] Thomas, F., Kozlov, A., and Corke, T., "Plasma Actuators for Cylinder Flow Control and Noise Reduction," *AIAA Journal*, Vol. 46, No. 8, 2008, pp. 1921–1931. doi:10.2514/1.27821

[37] Glezer, A., Amitay, M., and Honohan, A., "Aspects of Low- and High-Frequency Actuation for Aerodynamic Flow Control," *AIAA Journal*, Vol. 43, No. 7, 2005, pp. 1501–1511. doi:10.2514/1.7411

[38] Takeuchi, N., Yasuoka, K., and Ishii, S., "Inducing Mechanisms of Electrohydrodynamic Flow by Surface Barrier Discharge," *IEEE Transactions on Plasma Science*, Vol. 35, No. 6, 2007, pp. 1704–1709. doi:10.1109/TPS.2007.908909

[39] Boucinha, V., Magnier, P., Leroy-Chesneau, A., Weber, R., Joussot, R., Dong, B., and Hong, D., "Characterization of the Ionic Wind Induced by a Sine DBD Actuator used for Laminar-to-Turbulent Transition Delay," AIAA Paper 2008-4210, 2008.

[40] Sosa, R., Artana, G., Moreau, E., and Touchard, G., "Stall Control at High Angle of Attack with Plasma Sheet Actuators," *Experiments in Fluids*, Vol. 42, 2007, pp. 143–167.

doi:10.1007/s00348-006-0227-5
[41] Jolibois, J., Forte, M., and Moreau, E., "Application of an AC Barrier Discharge Actuator to Control Airflow Separation above a NACA 0015 Airfoil: Optimization of the Actuation Location Along the Chord," *Journal of Electrostatics*, Vol. 66, 2008, pp. 496–503. doi:10.1016/j.elstat.2008.03.008
[42] Enloe, C., McLaughlin, T., VanDyken, R., Kachner, K., Jumper, E., Corke, T., Post, M., and Haddad, O., "Mechanisms and Responses of a Single Dielectric Barrier Plasma Actuator: Geometric Effects," *AIAA Journal*, Vol. 42, No. 3, 2004, pp. 595–604. doi:10.2514/1.3884
[43] Corke, T., Post, M., and Orlov, D., "SDBD Plasma Enhanced Aerodynamics: Concepts, Optimization and Applications," *Progress in Aerospace Sciences*, Vol. 43, 2007, pp. 193–217. doi:10.1016/j.paerosci.2007.06.001
[44] Lin, J., and Dominik, C., "Parametric Investigation of a High-Lift Airfoil at High Reynolds Numbers," *Journal of Aircraft*, Vol. 34, No. 4, 1997, pp. 485–491. doi:10.2514/2.2217
[45] Falkenstein, Z., and Coogan, J., "Microdischarge Behaviour in the Silent Discharge of Nitrogen Oxygen and Water Air Mixtures," *Journal of Physics D: Applied Physics*, Vol. 30, 1997, pp. 817–825. doi:10.1088/0022-3727/30/5/015
[46] Benedict, L., and Gould, R., "Towards Better Uncertainty Estimates for Turbulence Statistics," *Experiments in Fluids*, Vol. 22, 1996, pp. 129–136. doi:10.1007/s003480050030
[47] Little, J., Nishihara, M., Adamovich, I., and Samimy, M., "High-Lift Airfoil Trailing Edge Separation Control Using a Single Dielectric Barrier Discharge Plasma Actuator," *Experiments in Fluids*, Vol. 48, 2010, pp. 521–537. doi:10.1007/s00348-009-0755-x
[48] Jukes, T. N., and Choi, K.-S., "Flow Control Around a Circular Cylinder Using Pulsed Dielectric Barrier Discharge Surface Plasma," *Physics of Fluids*, Vol. 21, 2009, Paper 084103. doi:10.1063/1.3194307
[49] Enloe, C., McLaughlin, T., Font, G., and Baughn, J., "Parameterization of Temporal Structure in the Single-Dielectric-Barrier Aerodynamic Plasma Actuator," *AIAA Journal*, Vol. 44, No. 6, 2006, pp. 1127–1136. doi:10.2514/1.16297
[50] Pons, J., Moreau, E., and Touchard, G., "Asymmetric Surface Dielectric Barrier Discharge in Air at Atmospheric Pressure: Electrical Properties and Induced Airflow Characteristics," *Journal of Physics D: Applied Physics*, Vol. 38, 2005, pp. 3635–3642. doi:10.1088/0022-3727/38/19/012
[51] Porter, C., Baughn, J., McLaughlin, T., Enloe, C., and Font, G., "Plasma Actuator Force Measurements," *AIAA Journal*, Vol. 45, No. 7, 2007, pp. 1562–1570. doi:10.2514/1.24497
[52] Hoskinson, A., Hershkowitz, N., and Ashpis, D., "Force Measurements of Single and Double Barrier DBD Plasma Actuators in Quiescent Air," *Journal of Physics D: Applied Physics*, Vol. 41, 2008, Paper 245209. doi:10.1088/0022-3727/41/24/245209
[53] Goksel, B., Greenblatt, D., Rechenberg, I., Nayeri, C., and Paschereit, C., "Steady and Unsteady Plasma Wall Jets for Separation and Circulation Control," AIAA Paper 2006-3686, 2006.
[54] Little, J., and Samimy, M., "Control of Separation from the Flap of a High-Lift Airfoil with DBD Plasma Actuation," AIAA Paper 2010-1088, 2010.
[55] Little, J., "High-Lift Airfoil Separation Control with Dielectric Barrier Discharge Plasma Actuators," Ph.D. Dissertation, Mechanical Engineering Department, Ohio State Univ., Columbus, OH, 2010.
[56] Amitay, M., and Glezer, A., "Controlled Transients of Flow Reattachment over Stalled Airfoils," *International Journal of Heat and Fluid Flow*, Vol. 23, No. 5, 2002, pp. 690–699. doi:10.1016/S0142-727X(02)00165-0
[57] Holmes, P., Lumley, J., and Berkooz, G., *Turbulence, Coherent Structures, Dynamical Systems and Symmetry*, Cambridge University Press, Cambridge, UK, 1996.
[58] Little, J., Nishihara, M., Adamovich, I., and Samimy, M., "Separation Control from the Flap of a High-Lift Airfoil Using DBD Plasma Actuation," AIAA Paper 2008-4200, 2008.
[59] Naim, A., Greenblatt, D., Seifert, A., and Wygnanski, I., "Active Control of a Circular Cylinder Flow at Transitional Reynolds Number," *Flow, Turbulence and Combustion*, Vol. 78, 2007, pp. 383–407. doi:10.1007/s10494-007-9068-4
[60] Benard, N., Jolibois, J., and Moreau, E., "Lift and Drag Performances of an Axisymmetric Airfoil Controlled by Plasma Actuator," *Journal of Electrostatics*, Vol. 67, 2009, pp. 133–139. doi:10.1016/j.elstat.2009.01.008
[61] Benard, N., and Moreau, E., "Electric Wind Produced by a Surface Plasma Discharge Energized by a Burst Modulated High Voltage," *Proceedings of the 29th ICPIG*, Cancun, 2009, pp. 1–4.
[62] Benard, N., and Moreau, E., "Capabilities of the Dielectric Barrier Discharge Plasma Actuator for Multi-Frequency Excitations," *Journal of Physics D: Applied Physics*, Vol. 43, 2010, Paper 145201. doi:10.1088/0022-3727/43/14/145201
[63] Lu, B., and Bragg, M., "Airfoil Drag Measurement with Simulated Leading-Edge Ice Using the Wake Survey Method," AIAA Paper 2003-1094, 2003.
[64] Zaman, K., and Culley, D., "Flow Separation Control over an Airfoil: Implication of Wake Velocity-Deficit Reduction," AIAA Paper 2008-3768, 2008.

L. Cattafesta
Associate Editor